Department of Physics and Astronomy
University of Heidelberg

Bachelor Thesis in Physics
submitted by

Christoph Aram Blattgerste

born in Minden (Germany)

2019

Study of different 180 nm HV-CMOS Implementations of the MuPix7 Pixel Sensor

This Bachelor Thesis has been carried out by

Christoph Aram Blattgerste

at the

Physics Institute in Heidelberg

under the supervision of

Prof. André Schöning

Abstract

The Mu3e experiment searches for the charged lepton flavor violating decay $\mu^+ \to e^+e^-e^+$ [1]. In the Standard Model of particle physics this decay is heavily suppressed with a branching ratio smaller than 10^{-55}. Therefore, an observation would be a clear sign for new physics. To reach the aimed sensitivity of one in 10^{16} decays, a novel detector technology is required to reach a high vertex and momentum resolution.

The Mu3e detector will be based on High-Voltage Monolithic Active Pixel Sensors (HV-MAPS) can be thinned to $50\,\mu$m. Furthermore, these sensors are produced in a commercial available High-Voltage-CMOS process.

In the scope of this thesis, an alternative HV-CMOS process for the production of MuPix sensors, HV-MAPS prototypes for Mu3e. Detailed characterizations of MuPix7, produced in the former standard process $H18$ by AMS and the studied High-Voltage process by TSI Semiconductors, show no significant differences between both used manufacturing processes. These results show that a production of the next MuPix iteration in the TSI process is feasible with a similar chip performance.

Zusammenfassung

Das Mu3e Experiment sucht nach dem geladenen Leptonfamilienzahl-verletzenden Zerfall $\mu^+ \to e^+e^-e^+$. Im Standardmodell der Teilchenphysik ist dieser Zerfall mit einem Verzweigungsverhältnis von weniger als 10^{-54} stark unterdrückt. Deshalb wäre ein beobachtetes Ereignis ein klarer Hinweis auf neue Physik. Um die Zielsensitivität von einem in 10^{16} Zerfällen zu erreichen, wird eine neue Detektortechnologie mit hoher Vertex- und Impulsauflösung benötigt.

Der Mu3e Detektor nutzt Hochspannungsbetriebene Monolithische Aktive Pixel Sensoren, HV-MAPS können bis auf $50\,\mu$m gedünnt werden. Außerdem können sie in einem kommerziellen 180 nm Hochspannungsbetriebenen CMOS, Verfahren gefertig werden.

In dieser Arbeit wird ein alternativer HV-CMOS Prozess für die Herstellung von MuPix Sensoren, HV-MAPS Prototypen für Mu3e, getested. Detaillierte Analysen des MuPix7, hergestellt im bisherigen Standardprozess $H18$ von AMS als auch im “High Voltage” Prozess von TSI Semiconductors, zeigen keine signifikanten Unterschiede zwischen den verwendeten Herstellungsverfahren. Dank dieser Ergebnisse, ist eine Produktion zukünftiger MuPix Sensoren im TSI Prozess bei bisher gemessener Chipperformance möglch.

Contents

page

I. Introduction 1

1. Introduction . . . 2
2. Standard Model of Particle Physics . . . 3
3. The Mu3e Experiment . . . 5
   - 3.1. Muon Decay . . . 5
   - 3.2. Experimental Situation . . . 6
   - 3.3. Detector Concept . . . 7
4. Semiconductor Physics . . . 9
   - 4.1. Semiconductor . . . 9
   - 4.2. Doping . . . 9
   - 4.3. PN-junction . . . 10
   - 4.4. Transistor Manufacturing . . . 11
5. Particle Interactions with matter . . . 14
   - 5.1. Particle Detection . . . 14
   - 5.2. Scattering . . . 15
6. Pixel Sensors . . . 16
   - 6.1. Hybrid Pixel Sensors . . . 16
   - 6.2. MAPS . . . 16
   - 6.3. HV-MAPS . . . 16

II. MuPix7 + Setup 18

7. MuPix7 . . . 19
   - 7.1. Clocking . . . 20
8. The Test Setup . . . 22
   - 8.1. PCB / Insert . . . 22
   - 8.2. Timing Reference . . . 23
   - 8.3. Firmware / Software . . . 24
9. Measurement Techniques . . . 26
   - 9.1. Climate Chamber . . . 26
   - 9.2. Radioactive sources . . . 26
   - 9.3. Threshold Scan . . . 26

9.4. Time-over-Threshold 27

III. Measurements 29

10. Commissioning of the Setup and the TSI chip 30
    10.1. Temperature dependence 31
    10.2. Injection gauging 32
11. Direct Comparison: AMS vs. TSI 34
    11.1. Diode 34
    11.2. Signal amplification 36
    11.3. SNR measurement 37
    11.4. Characterization of the PLL 41
    11.5. Time Resolution 45
    11.6. Power Consumption 49
    11.7. LVDS Readout 50
    11.8. Global Bias Current 51

IV. Discussion & Outlook 56

12. Summary & Discussion 57
13. Outlook 58

V. Appendix 59

Part I.

Introduction

1. Introduction

The Standard Model of particle physics (SM) summarizes all known elementary particles which form matter and mediate forces. Although this model has been verified by several experiments [2, 3, 4], the theory can be further extended. Extensions to the SM allow massive neutrinos and lepton flavor violating processes.

Situated at the Paul-Scherrer-Institut (PSI) in Switzerland [1], the Mu3e experiment searches for the charged lepton flavor violating (cLFV) decay $\mu^+ \rightarrow e^+e^-e^+$. Since the SM predicts a non-measurable branching ratio smaller than 10^{-55} [5], Mu3e was designed to probe physics beyond the Standard Model at the high intensity frontier with an aimed final sensitivity of one signal in 10^{16} muon decays at 90% confidence level.

To achieve the required background suppression and reduce multiple Coulomb scattering, High-Voltage Monolithic Active Pixel Sensors (HV-MAPS) [6] are chosen. These sensors are fully integrated, can be thinned to $50\,\mu$m which allows the construction of a low material budget detector with high vertex and momentum resolution. Furthermore, fast charge collection via drift is obtained in the reversely biased diode. The applied high voltage ensures a high rate capability and a high efficiency.

The production process of a foundry affects the performance of silicon chips. For proper qualification, the well characterized HV-MAPS prototype, MuPix7, produced by Austria Micro Systems (AMS) [7], was resubmitted with TSI Semiconductors [8]. Within this thesis, sensors produced in the so called High Voltage process by TSI are studied as an alternative to the used AMS $aH18$ process. Both processes are based on the same commercial International Business Machines Corporation (IBM) 180 nm HV-CMOS process and are expected to perform similar. The sensors are produced with identical 180 nm sensor design and investigated with the same experimental setup. Therefore, the measured deviations can be corrected by adjusting the chip configuration for future MuPix versions.

2. Standard Model of Particle Physics

The Standard Model of particle physics combines three of the four known fundamental interactions in a quantum field theory. All known matter is formed out of 12 half-integer spin particles called fermions and their corresponding antiparticles. Interactions are mediated by integer spin particles called bosons depicted in figure 2.1.

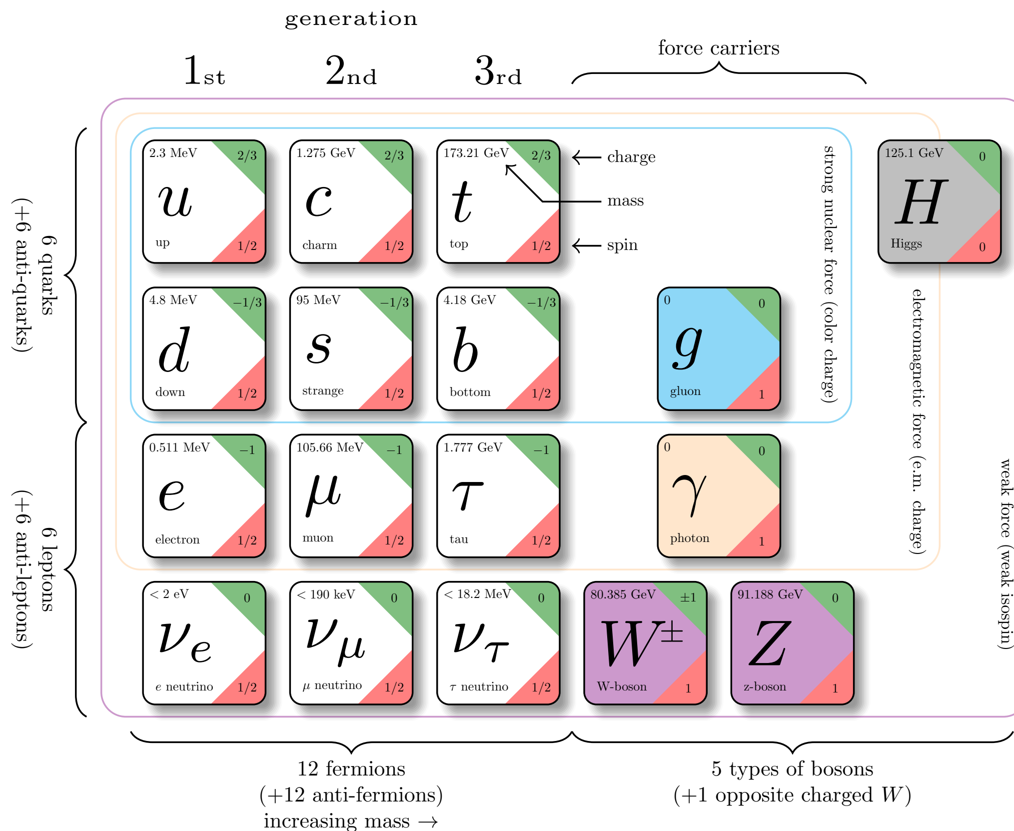

Figure 2.1.: The Standard Model of particle physics [9].

For quantum electrodynamics (QED), the mediating boson is the photon γ. It is massless and not electrically charged, but couples to every charged particle. In the weak interaction, there exist three mediators, two electrically charged bosons W^+/W^- and the neutral Z^0. W^+/W^- are the only bosons, allowing generation and flavor changes. On high energy scales, QED can be unified with the weak interaction to the electroweak interaction. Quantum chromodynamics (QCD) describes the

strong interaction mediated by massless gluons g. They are not electrically-, but color charged and couple to quarks and themselves in self-coupling.

The last boson of the SM is the Higgs boson. The Higgs mechanism [10] describes interactions of the other SM particles with the Higgs field, giving them their mass.

Fermions are divided into two groups, quarks and leptons. There are three different generations per group, classified according their mass. Each quark generation consists of two quarks, one with an electric charge of $+2/3$ and the other one with a charge of $-1/3$. Every quark carries color charge, but only exists in color-neutral confined states.

The other group, leptons, do not interact strongly. Three leptons are electrically charged whereas the other three leptons, neutrinos ν, are neutral. Following the three generations, there are the charged electron e, muon μ and tauon τ with increasing mass. Neutrinos do not undergo neither strong nor electromagnetic interaction. Only bosons of the weak interaction couple directly to them. All six leptons have a quantum number called lepton flavor specifying their generation.

For each particle, there is a corresponding antiparticle. They have opposite quantum numbers such as electric charge and can equalize their complement.

To be complete, general relativity which declares gravity as fourth fundamental interaction can not yet be covered by the SM. The graviton as mediator is theoretically predicted, but has not been observed yet.

Neutrino experiments performed for example at the Super Kamiokande Observatory [11] and the Sudbury Neutrino Observatory [12] showed a significant violation of lepton flavor, not predicted in the SM. Due to neutrino oscillations, suggesting massive neutrinos, the SM is extended to the "Neutrino Standard Model of Particle Physics" (νSM) [13].

However, the νSM does not answer all questions. Dark matter, the expanding universe or the matter-antimatter asymmetry are just a few examples. Theories beyond the Standard Model (BSM) try to explain these phenomena, but so far no indications for new physics have been found.

3. The Mu3e Experiment

In the νSM, massive neutrinos can change the lepton family number and thus, violate the lepton flavor conservation. The Mu3e experiment aims to discover the same effect for charged leptons. The observation of the highly suppressed decay $\mu^+ \to e^+e^-e^+$ would already be a sign for BSM physics.

3.1. Muon Decay

According to the SM and observations, the Michel decay occurs most likely with a branching ratio (BR) of nearly 100% as the simplest conversion from a muon into an electron:

$$\mu^+ \to e^+\nu_e\bar{\nu_\mu} \tag{3.0}$$

The same decay can also occur with an internal production of electron positron pairs (see figure 3.1a). This tree-level decay also conserves lepton flavor, but is less likely with a BR of $(3.4 \pm 0.4) \times 10^{-5}$ [14].

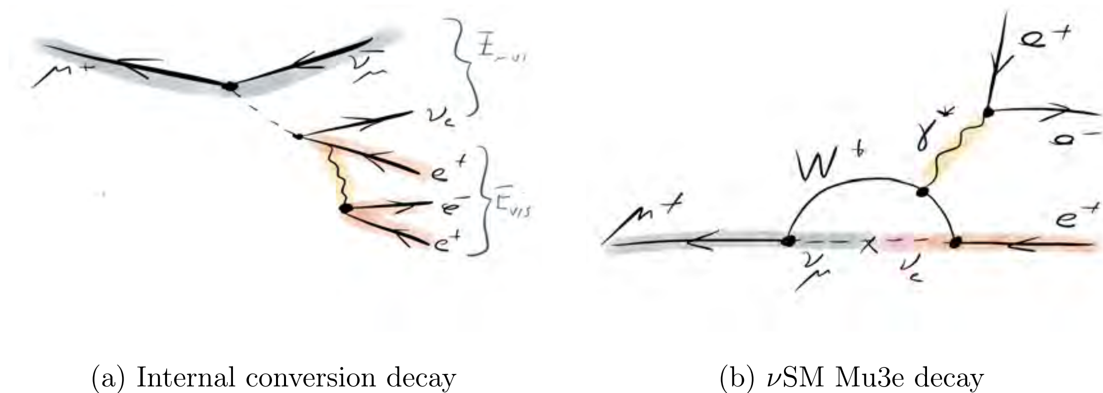

(a) Internal conversion decay

(b) νSM Mu3e decay

Figure 3.1.: Examples for a muon decaying into three electrons and two neutrinos at tree level (a) and in the electrons at loop level (b)

In the νSM, charged lepton flavor violating (cLFV) decays appear at loop-level and are heavily suppressed. The Feynman diagram of the decay

$$\mu^+ \to e^+e^-e^+ \tag{3.1}$$

with neutrino oscillation is sketched in figure 3.1b. The BR smaller than 10^{-55} was calculated in [5] and is non-observable.

In BSM theories, the cLFV decay mode can be enhanced. Thus, an observation of the decay $\mu^+ \to e^+e^-e^+$ is a clear sign for physics beyond the SM.

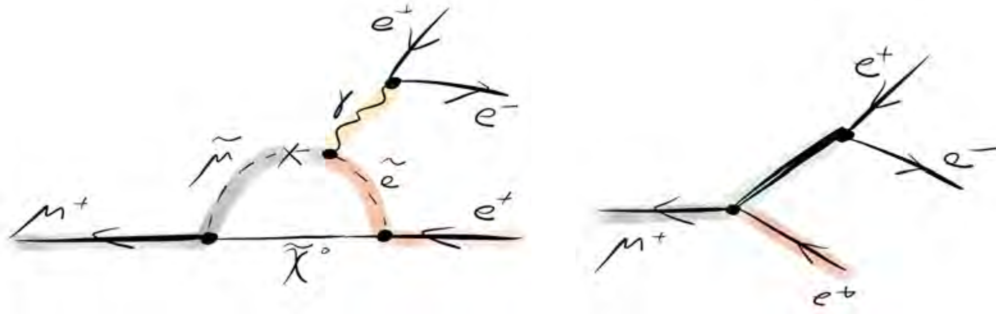

(a) Loop-level decay with SUSY particles

(b) Decay on tree-level.

Figure 3.2.: Examples for $\mu^+ \to e^+e^-e^+$ via BSM decay modes

BSM theories such as supersymmetric (SUSY) theories predict other virtual particles involved in the muon decay. The neutrino line can be replaced with a SUSY particle at loop-level visualized in the Feynman diagram 3.2a. It is also conceivable that an unknown mediator is involved coupling to a muon and an electron at tree-level as shown in sketch 3.2b.

For the Mu3e experiment, decays with detector signals similar to $\mu^+ \to e^+e^-e^+$ as internal conversion are background decays and have to be discriminated.

3.2. Experimental Situation

For different cLFV muon decay channels, previous experiments set limits with lower sensitivity depicted in figure 3.3. Future experiments as Mu3e will further reduce the sensitivity limit by orders of magnitude.

The SINDRUM experiment searched for the decay $\mu^+ \to e^+e^-e^+$ at Paul-Scherrer-Institut (PSI). The upper limit for the BR was set to $< 10^{-12}$ at a confidence level (CL) of 90% in 1985 [16].

Later on, the MEG experiment, also situated at PSI, searches for the decay $\mu^+ \to e^+\gamma$ since 2008. Out of 7×10^{14} muons stopped, the upper limit for the BR was calculated to $< 4.2 \cdot 10^{-13}$ at a CL of 90% in 2016 [17].

The SINDRUM II experiment covers an other $\mu^- \to e^-$ conversion process where the decay in muonic gold atoms was investigated. The BR relative to the nuclear capture probability was determined to $B_{\mu e}^{Au} < 7 \cdot 10^{-13}$ from 2006 [18]. Two other experiments searching for the same conversion are already planned, COMET in Japan at J-PARC and Mu2e at FermiLab with a planned BR sensitivity of $10^{-16} - 10^{-17}$ at a CL of 90% [19].

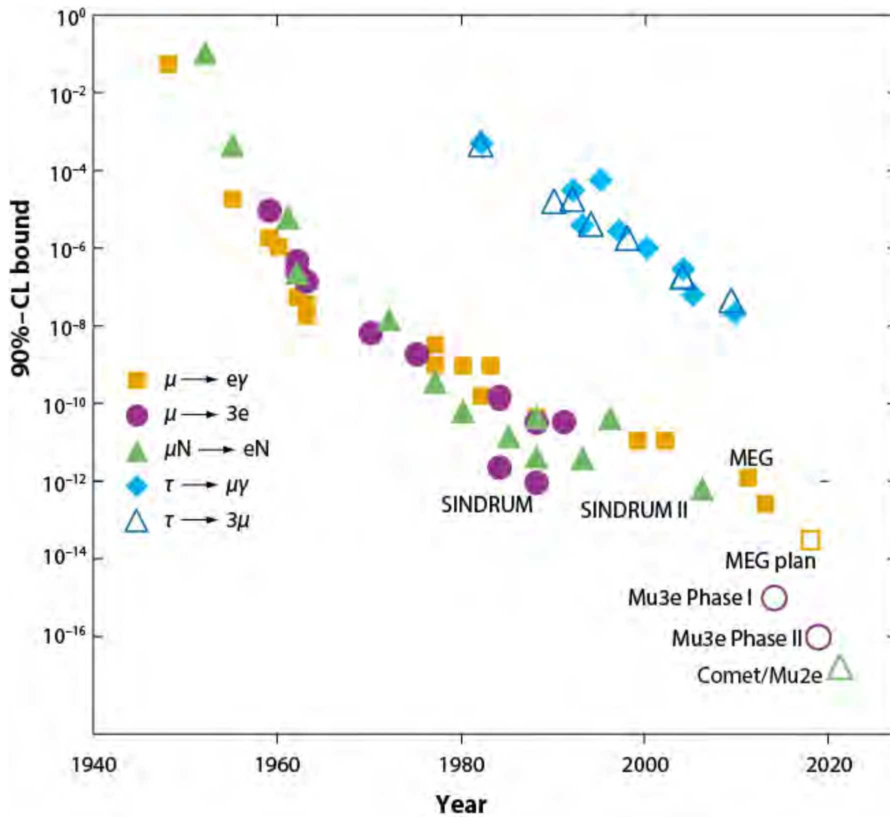

Figure 3.3.: History of charged lepton flavor violation searches with realized (filled markers) and planned (empty markers) experiments from [15]

3.3. Detector Concept

Muons with an energy of 4 MeV decay at rest at a hollow double cone target produced of Mylar [1] depicted in figure 3.4. The following equations describe the kinematics of the signal decay with index i for all final state particles:

$$\vec{p}_{tot} = \sum_i \vec{p}_i = 0 \tag{3.3}$$

$$E_{tot} = \sum_i E_i = m_\mu c^2 \approx 105.7\, MeV \tag{3.3}$$

For track reconstruction, a homogeneous magnetic field of 1 T is generated by a solenoid magnet. Due to the bended particle track, a momentum with resolution below 0.5 MeV/c is determined for each particle.

To reach the aimed sensitivity, the signal decay described in 3.1 has to be distinguished from background. However, irreducible background decays do not

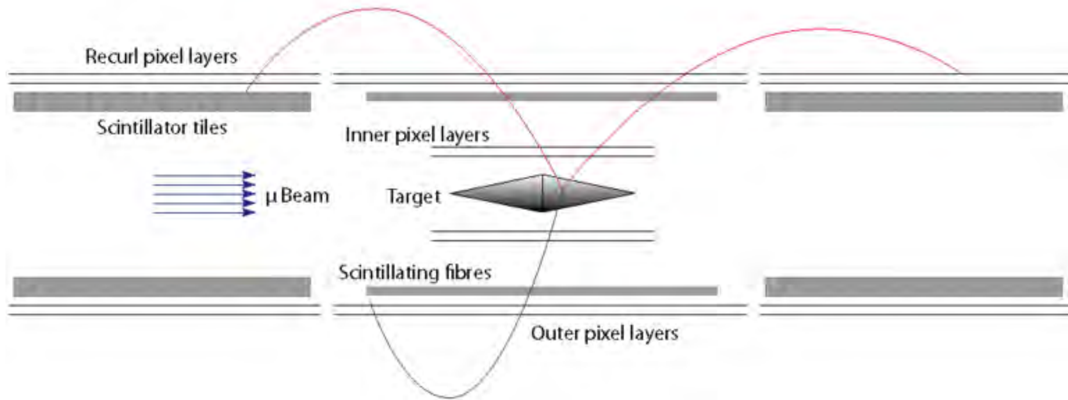

Figure 3.4.: The mu3e detector tube sketched in parallel to the beam

fulfill equation 3.3 because of undetected neutrinos. Two simultaneously decaying narrow particles can accidentally be combined to the decay-of-interest. High momentum and vertex resolution are needed to discriminate these background processes, quantified in [1].

For optimal track fitting, the detector is separated into an inner and an outer layer with two layers of sensors each, see sketch 3.4. The inner layer is placed as close as possible to the target for a precise extrapolation the interaction point. Additional layers are added, in order to reduce multiple Coulomb scattering as source of inaccuracy for low-momentum electrons with $p < 53\,\mathrm{MeV/c}$ (half the muon rest mass). The outer layer and recurl layers on both sides of the central pixel tracker are placed such that most particles perform a half circle. All pixel layers together will have a dimension of 1.20 m length and 0.2 m diameter.

For precise time information, scintillating tiles and fibres are added. They provide additional time resolution for a better background suppression.

In phase II, 10^9 muons per second will be provided which is possible with the upgraded beamline at PSI [1]. Thus, this is the only facility where Mu3e can reach the aimed branching ratio sensitivity of 1 decay in 10^{16} in a reasonable time.

4. Semiconductor Physics

4.1. Semiconductor

Experimentally, semiconductors are defined as materials with a conductance $\sigma \approx 10^{-8}...10^{3}(\Omega\,\mathrm{cm})^{-1}$. At temperature $T = 0\,\mathrm{K}$, they are insulators, but semiconductors become conducting at higher temperatures explained by the band theory, discussed in detail in [20]. For free atoms, energy levels of electrons exist in discrete form. In a crystal, atoms are placed close enough that neighboring electron orbits interfere. This means for N atoms in the crystal, each electronic state of an atom is then split into N states referred to as energy bands. The energy difference electrons have to pass between these levels defines the band gap. For the electronic properties, only the two outer bands are important, because completely filled bands do not contribute to the conductivity. The valence band is the outermost band filled with electrons in the ground state. The conductance band denotes the next higher energy level. The Fermi energy E_F is defined as the highest energy an electron has in the ground state. For temperatures $T > 0\,\mathrm{K}$, the Fermi distribution $f(E)$, fraction of electrons per available energy state, is not a sharp step-function anymore, but a smoothed sigmoid curve shown in figure **??**. This means that electrons also occupy higher energy states plotted as energy E divided by the thermal energy $E_T = k_B T$. Excited electrons leave behind vacancies in the valence band, called holes. In semiconductors with a small band gap, electrons can easily be thermally excited and contribute to the semiconductors conductivity. The more free charge carriers are available, the higher is the conductivity σ:

$$\sigma = e \cdot (n\mu_e + p\mu_p) \tag{4.0}$$

where n and p are the charge densities for electrons (n-type carriers) and holes (p-type carriers), e is the elementary charge and $\mu_{e/p}$ denote the carrier mobilities, see table 4.1.

4.2. Doping

In order to modulate the resistivity of a semiconductor, the conductivity can be adjusted through doping. Doping is the process of implementing impurities into a semiconductor, hence, disturbing the crystal structure.

Other elements with three or five electrons on their outer shell are used to adjust the number of free charge carriers. An electron donor has one more outer electron which is not bonded with neighboring atoms. This additional charge carrier can easily be excited to the conductance band which results in a higher conductivity. Materials with only three outer electrons, acceptors, leave a hole in the crystal

Property	**value**	**Unit**
Atomic number Z	14	
Atomic weight	28.09	
Crystal structure	Diamond	
Intrinsic charge density	1.5×10^{10}	$1/\text{cm}^3$
Dielectric constant ϵ_r	11.9	
Indirect band gap (300K)	1.12	eV
Average creation energy for an electron-hole pair E_{ep}	3.66	eV
Eletron mobility μ_e	1450	$\text{cm}^2\text{s/V}$
Hole mobility μ_p	500	$\text{cm}^2\text{s/V}$

Table 4.1.: Silicon properties at 300 K adopted from [21]

structure acting like a positive charge carrier. Depending on the material, the semiconductor is p-doped for an acceptor, or n-doped for a donor.

4.3. PN-junction

A p-doped area connected to an n-doped one forms the simplest semiconducting component, a pn-junction known as diode.

Around the boundary, the depletion zone, electrons recombine with holes in a thermal diffusion process, leaving behind immobile doped ions in the lattice. These ions induce an electric field which forces electrons and holes to a drift movement contrary to the diffusion. In thermal equilibrium, both processes, thermal diffusion and drift, equalize each other.

Because of the separated charge carriers, a diffusion voltage U_D is generated with an energy difference of eU_D between valence- E_v and conductance energy level E_c. In thermal equilibrium, the Fermi energy E_F adjusts globally, shown in figure **??**.

The width of the junction with changing potential depends on the thermal voltage, and the doping concentration of both doped semiconductors. The thickness d of the depletion zone is the sum of the expansion in both doped materials x_n and x_p with the doping concentration of acceptor/donor atoms N_A/N_D and the vacuum permittivity ϵ_0 according to [20].

$$d = x_n + (-x_p) = \sqrt{\frac{2\epsilon_0 \epsilon U_0}{e} \frac{N_A + N_D}{N_A \cdot N_D}} \tag{4.1}$$

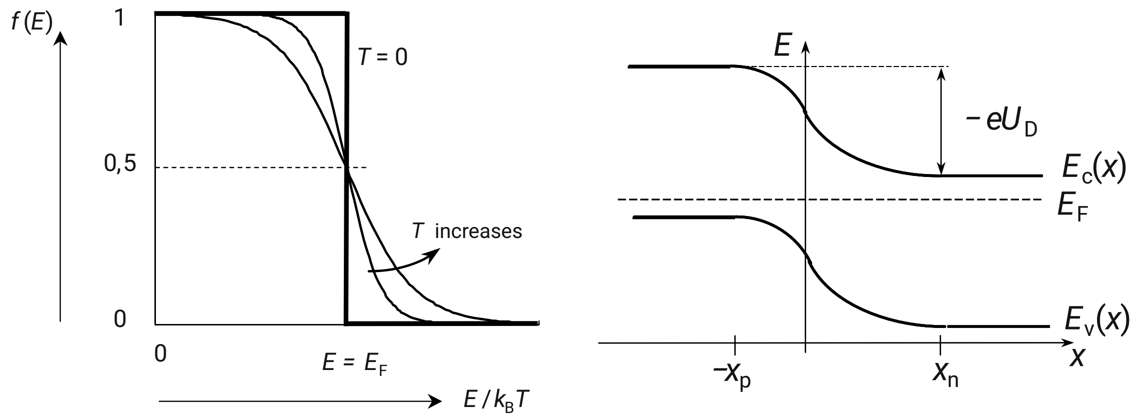

Figure 4.1.: Fermi distribution (a) and energy levels (b) of a pn-junction.

Depending on its polarity, a positive or negative applied bias voltage U_0 enlarges or shrinks the depletion zone. A forward biased diode gets conducting, whereas a reverse bias generates an even stronger electric field against the applied current flow. For a doping $N_A \ll N_D$, the formula for the thickness of the depletion zone can be simplified:

$$d \propto \sqrt{U_0/N_A} \tag{4.1}$$

The capacitance C of a diode approximately behaves like a parallel plate capacitor and can be expressed via the depletion width d in a material with relative permittivity ϵ_r:

$$C = A\sqrt{\frac{eN_A\epsilon_0\epsilon_r}{2U_0}} \tag{4.1}$$

4.4. Transistor Manufacturing

For more complex circuits, pn-junctions and other semiconducting components are combined. Further information on the functionality of transistors and other electronic components can be found in [22] or in [23].

Before a transistor can be manufactured in hardware, the designed circuitry has to be adapted according to the foundry's design rules (DR). This might cause most differences between two foundries if the original design was adjusted differently. These DR are geometric constraints ensuring the production reliability and the correct functionality. As example, two generic DRs set the minimal width of

conducting lines and the minimal spacing to one another. Different distances cause different electric field strengths shown in [24].

After several iterations with functionality checks, the design is printed as photosensitive masks. They are used for photolithography as the partial removal of one slice of material in order to create a complex structure. For a three dimensional structured sensor, applying a material and photolithography are repeated multiple times.

In the first production step, the needed material is evaporated through gas diffusion or injected through ion implantation on top of the substrate shwon in figure 4.2a. On top, a light-sensitive material, called photoresist is applied to the substrate. There are positive and negative photoresists which behave contrary under light irradiation. Under light irradiation, the unmasked parts of the positive photoresist are removed and the underlying doped material is exposed as seen in figure 4.2 b&c. Furthermore, the photoresist is chosen such that it endures etching and saves the underlying material depicted in sketch 4.2 d&e. After etching, the evaporated doped material only stays in the regions with applied photoresist while the other parts are removed. Finally, the photoresist is removed by abrading the uppermost layer, called polishing (see figure 4.2 f).

The final wafer contains many finished chips side by side and has to be diced to obtain a single sensor. This procedure might also affect the sensor performace, but is not part of this investigation.

Differences between foundries can occur through the use of differently doped substrates, different applied insulators or different conducting materials. Slightly dffering conducticities affect a measurable difference in the characteristics of a microelectronic circuitry. Furthermore, the precision of the photolithography plays a role because the material might not be completely removed. These geometrical uncertainties affect the electrical field and the conductivity causing a sensor behaviour differing from the designed one.

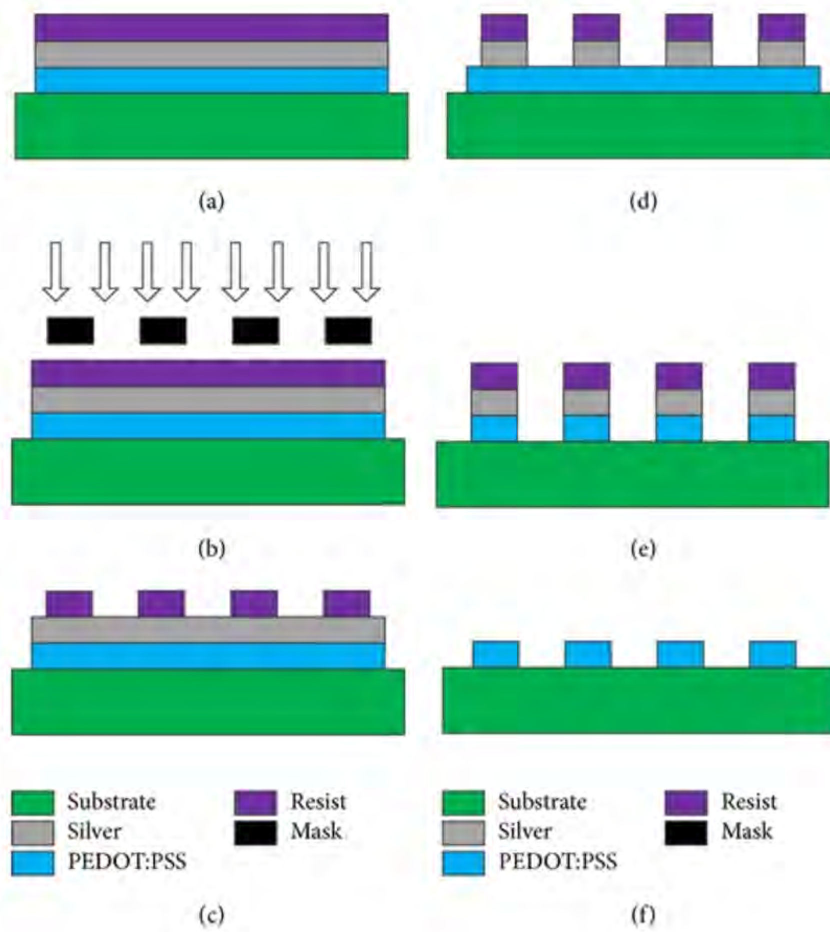

Figure 4.2.: Photolithography with exposure with masking (b), etching (d) and polishing (f) [25]

5. Particle Interactions with matter

The type and probability of an interaction with matter depends on the incoming particle and its energy. The main energy loss, ionization, is discussed for heavy as well as light charged particles.

The mean energy loss by ionization per distance in a medium for charged particles with masses $\geq 100\,\mathrm{MeV}$ is described by the Bethe-Bloch-formula [26].

For light charged particles, other processes such as Bremsstrahlung contribute and require a different formula. The mean energy loss of positrons and electrons per distance is described by the Berger-Seltzer equation 5.0, established in 1984 [27]. For an electron/positron with speed $\beta = \frac{v}{c}$ and a rest energy of $m_e c^2$ traveling a distance x into a target of density ρ, atomic number Z and relative atomic mass A, the formula reads:

$$\left\langle \frac{dE}{dx} \right\rangle = \rho \frac{0.15}{\beta^2} \frac{Z}{A} \Big(B_0(p) - 2 \log \frac{I}{m_e c^2} - \delta \Big) \tag{5.0}$$

Here, I is the mean excitation potential, $B_0(p)$ the momentum dependent stopping power and δ the density-effect correction for the material. The mean energy loss for electrons and positrons slightly differs as shown in figure 5.1. This is due to the indistinguishability of incoming electrons and electrons within the material atoms.

Beside massive particles, also photons produce a detectable signal in a pixel sensor. If the energy of a photon is higher than the electron binding energy, photoionization occurs. Thereby, an electron is kicked onto the conductance band of a diode. Thus, a signal is generated. Multiple photoionization is very unlikely, but observable for higher light intensities. Here, multiple photons together provide the energy to release a single electron from its nucleus. For the following measurements, a radioactive ^{55}Fe source is used with gamma rays. The photon's mean energy of $5.9\,keV$ triggers about 1600 free electrons in a pixel.

5.1. Particle Detection

For the detection of a particle, an interaction with the sensor material is necessary. An interaction is detectable if the deposited energy is high enough to produce an electron-hole pair. The more interactions take place, the higher is the signal amplitude. However, signal detection is always a trade between high detection efficiency and disturbing the measured particle via energy loss and multiple Coulomb scattering.

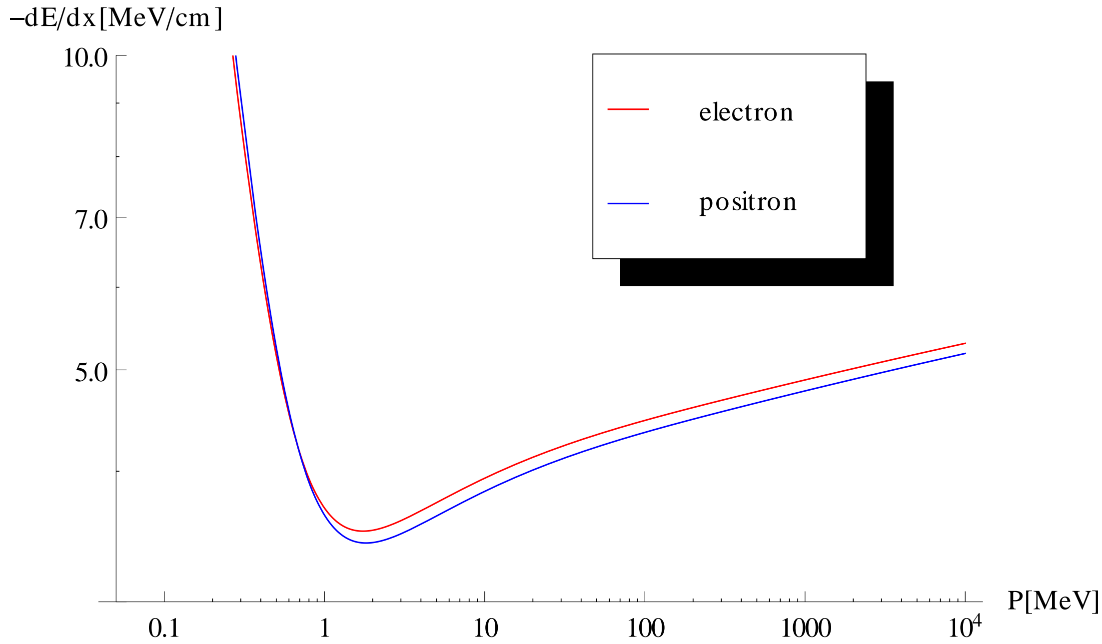

Figure 5.1.: Berger Seltzer formula for electrons and positrons according to 5.0 taken from [28]

5.2. Scattering

According to Newton's third axiom, any interaction with the sensor also causes a deflection of a crossing particle. The sum over all tiny scattering processes in the sensor layer results in a mean scattering angle Θ_{plane}. This angle is dominated by interactions between an incoming particle and the sensor nuclei's Coulomb field. Multiple Coulomb scattering processes can be approximated by a Gaussian distribution and its mean root square [26].

$$\Theta_{RMS} = \frac{13.6\,\text{MeV}}{\beta c p} z \sqrt{\frac{x}{X_0}} \cdot \left[1 + 0.038 \log \frac{x}{X_0}\right] \tag{5.1}$$

Because of the reciprocal dependence of the particles velocity $\beta = \frac{v}{c}$ and momentum p, slow particles are scattered more. This can be equalized with a reduction of the sensor thickness in units of the radiation length $\frac{x}{X_0}$. Regarding equation 12, HV-MAPS are very thin to account for the requirements of low momentum particles.

6. Pixel Sensors

Out of the presented pn-junctions, pixel sensors can be build. The observation of a crossing particle makes use of ionization. The pixel technology, in general, allows for a good spacial resolution.

6.1. Hybrid Pixel Sensors

Hybrid pixel sensors are widely used in particle physics and explained in detail in [29]. A pixelated active diode array is solder-bump-bonded to a readout application specific integrated circuit (ASIC). This design enables the optimization of both sensors separately on different substrates. However, hybrid pixel sensors need a high material budget which heavily scatters low energetic particles and reduces the spacial resolution. Furthermore, the bump bonding method of each pixel is quite expensive and technically challenging for small pixel sizes.

6.2. MAPS

Monolithic active pixel sensors (MAPS) present a cost efficient alternative based on common active pixel sensors. Contrary to hybrid sensors, the bonding process is obsolete due to the monolithic design. MAPS implement the pixel, where charge is collected via diffusion, and readout parts on the same chip. This allows for a thinned sensor with only 0.1% radiation length reducing multiple Coulomb scattering. No bonding is necessary and the cheap commercial Complementary Metal-Oxide-Semiconductor (CMOS) procedure can be used.

6.3. HV-MAPS

The concept of High-Voltage Monolithic Active Pixel Sensors (HV-MAPS) was firstly introduced in [30]. It combines the MAPS technology with a high voltage reverse biased diode.

In addition to the monolithic approach, the applied high voltage speeds up the charge collection via drift. Thus, created electron-hole pairs are exhausted in less than 1 ns via the strong electric field. Applying a reverse biased high voltage up to −100 V between the deep n-well and the p-substrate also enlarges the depletion zone towards MAPS. Due to the larger sensitive area in each pixel following equation 4.1, more particles are detected in the depletion zone and a higher rate is measured.

Despite the fast charge collection, a mean efficiency above 99 % is reached, according to [31]. Further details can be found in section 7.

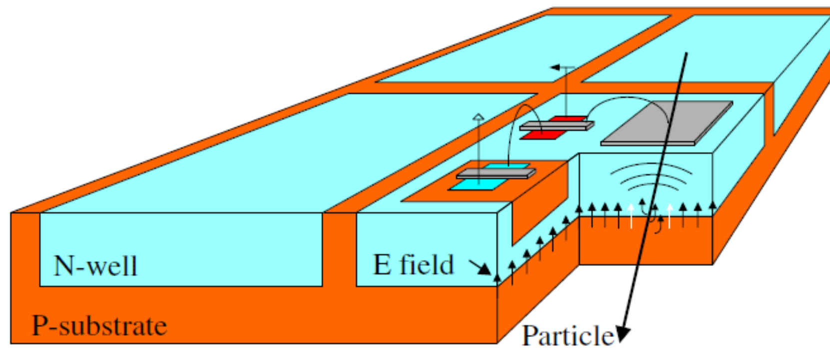

Figure 6.1.: A pixel combines a diodes depletion zone with in pixel electronics [6]
.

For manufacturing, a commercial available High Voltage-CMOS procedure can be used.

Part II.

MuPix7 + Setup

7. MuPix7

In the course of this thesis, the first fully integrated MuPix prototype, the MuPix7, is investigated. The active area of MuPix7 spans $\sim 3.3 \times 3.2\, mm^2$ and has an active matrix of 32×40 pixels. Each pixel has a dimension of $\sim 103 \times 81\, \mu m^2$ and consists of 3×3 diodes. This segmentation is done to decrease the capacitance and therefore lower the noise [32]. Figure 7.1 illustrates the sensor with one single pixel highlighted and the point-to-point connection to its periphery cell. Desirable for good coverage is a low amount of dead material meaning a good ratio of active area to periphery, so $380\mu m/3294\mu m = 11.5\%$ [33].

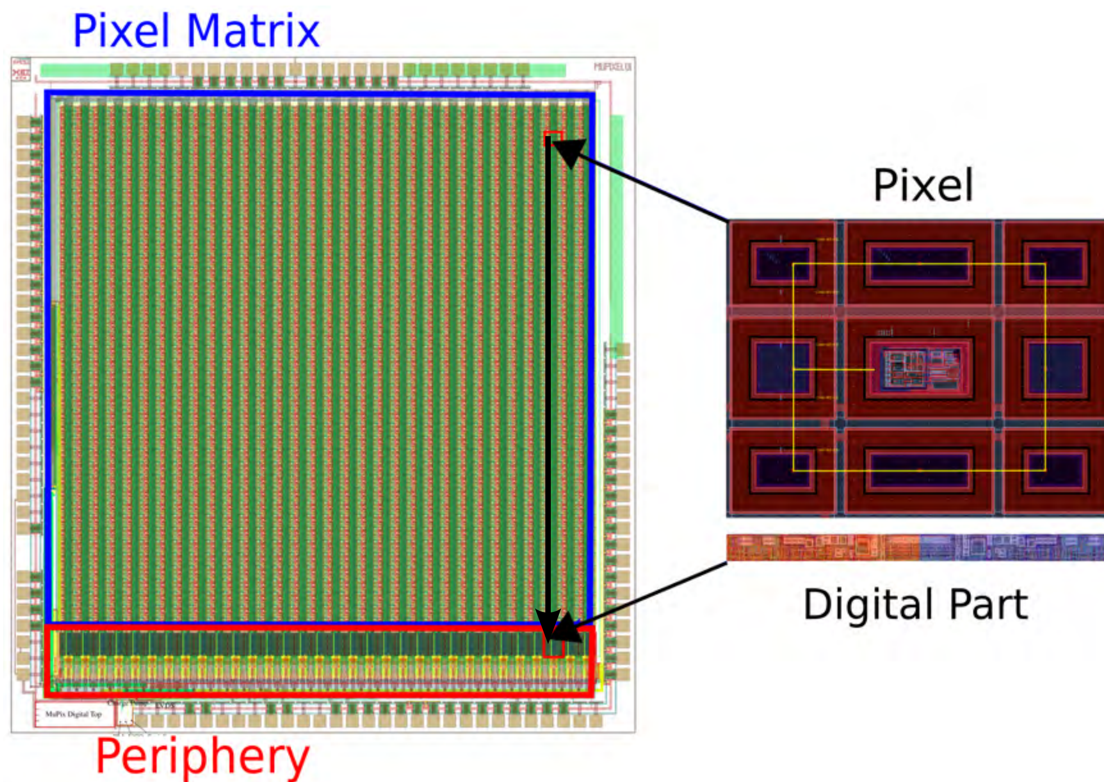

Figure 7.1.: Sketch of the matrix' architecture with a single pixel with its digital part highlighted.

Hit signals from each pixel are processed according to figure 7.2. Following the diode, a capacitor collects all deposited charge. In addition, an injection current can be induced to simulate a traversing particle. The generated voltage peak is amplified by a charge sensitive amplifier (CSA) directly within each pixel.

For further signal processing, a source follower drives the signal to a point-to-point connected periphery cell where it gets further amplified. The signal is

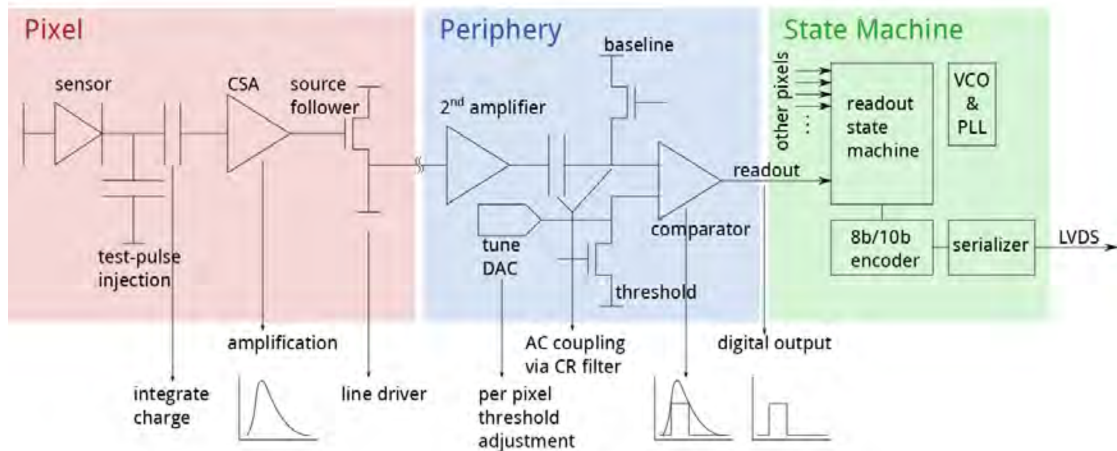

Figure 7.2.: Processing steps beginning with a sensor signal in the MuPix7.

modulated onto a baseline (BL) voltage of 0.8 V and discriminated in the following comparator. If the modulated signal gets higher than the constant threshold voltage, the comparator generates a normalized digital pulse.

The pixels are read out zero suppressed and the data is serialized by the on-chip state machine. The digital data stream is 8b/10b encoded and sent out via a Low Voltage Differential Signal link with 1.25 Gbit/s [34].

7.1. Clocking

The clock signal is generated in the phase-locked-loop (PLL) investigated in section 11.4.

A reference signal of 125 MHz is provided externally by the FPGA to which a voltage-controlled-oscillator (VCO) is synchronized. A VCO generates a clock signal depending on the applied voltages VPVCO and TOVCO. The phase of the signal is compared to the reference clock signal in the phase detector (PD). There, a patch signal is produced in alternating current. After conversion into a direct current in the charge pump, the patch is feed back into the VCO. The self-regulated loop has a final frequency of 625 MHz according to [28].

According to the different usages of the clock, slower clocks are generated out of the stable clock using cloc dividers as shown in figure 7.3. Main applications are the control of the readout state machine and the generation of hit timestamps. A

digital clock of 125 MHz has a period duration between two rising edges of 16 ns. Therefore, the used 8 bits for a timestamp are sufficient to cover 4 µs. After this time a hit is expected to be read out by the state machine at latest.

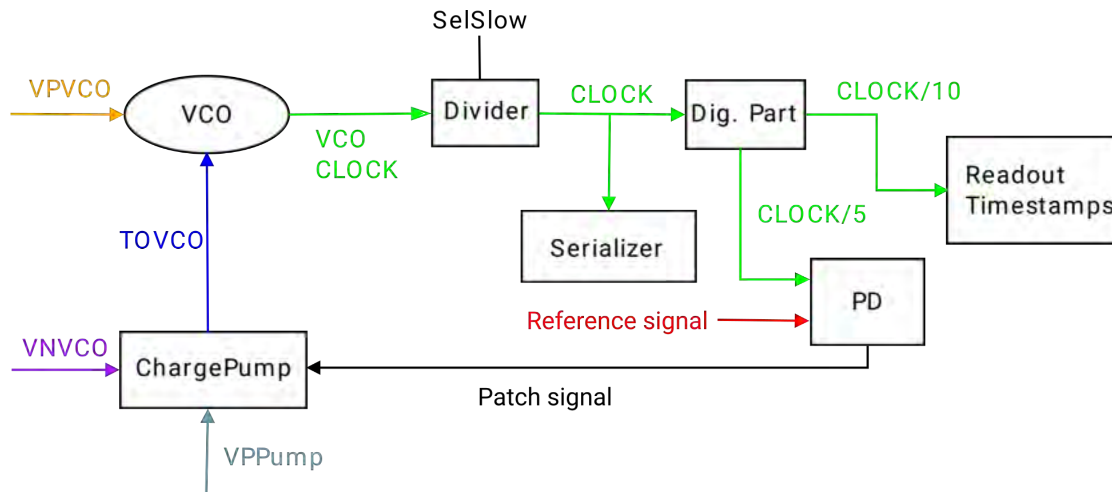

Figure 7.3.: Sketch of the on-chip clock circuitry [28].

8. The Test Setup

For detailed testing, MuPix7 is housed by the MuPix8 v2 test-board PCB. Data are routed to a Field-Programmable Gate Array (FPGA) where multiple sensors can be combined and controlled. Finally, the data are handled by a data acquisition system (DAQ) and monitored by a custom graphical user interface (GUI) on a commercial PC see section 8.3 and in [35].

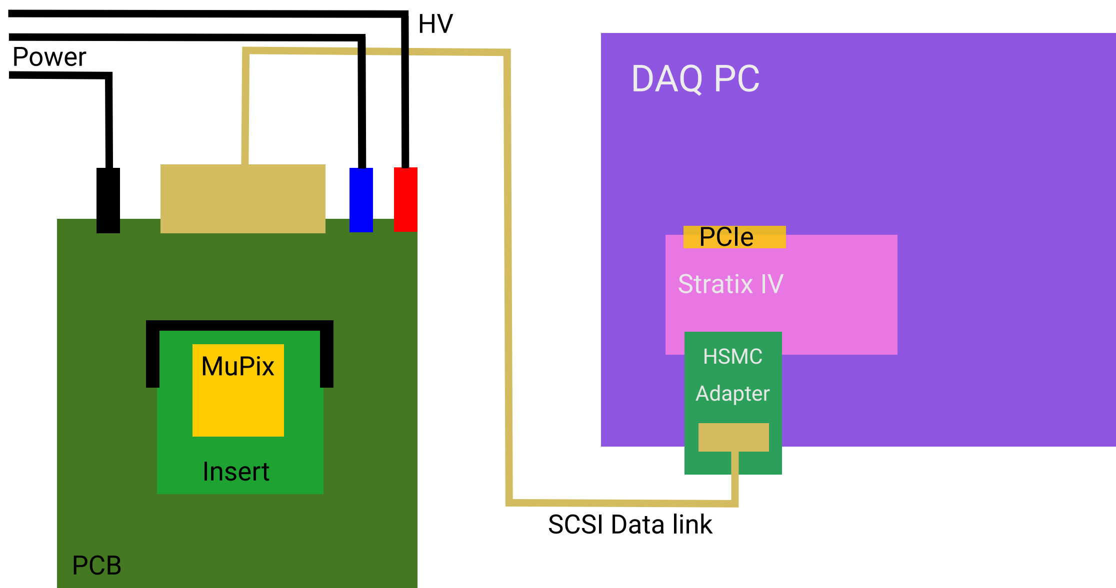

Figure 8.1.: Sketch of the MuPix7 single setup.

8.1. PCB / Insert

Figure 8.1 shows all units of a test-setup. The golden rectangle marks the MuPix7 chip itself. For testing, the sensor is wire bonded to an insertable PCB, called insert (light green rectangle) [36]. On the insert, a last filtering of the desired voltages takes place and several test-points are provided.

In order to reduce the systematical errors, the insert is plugged into the MuPix8 v2 PCB (dark green rectangle) shown in figure 8.2. The PCB generates the voltages and injection pulses for the chip and routes the data links to the external FPGA. For data in- and output of the chip, the PCB has a Small Computer System Interface (SCSI) connection to the FPGA.

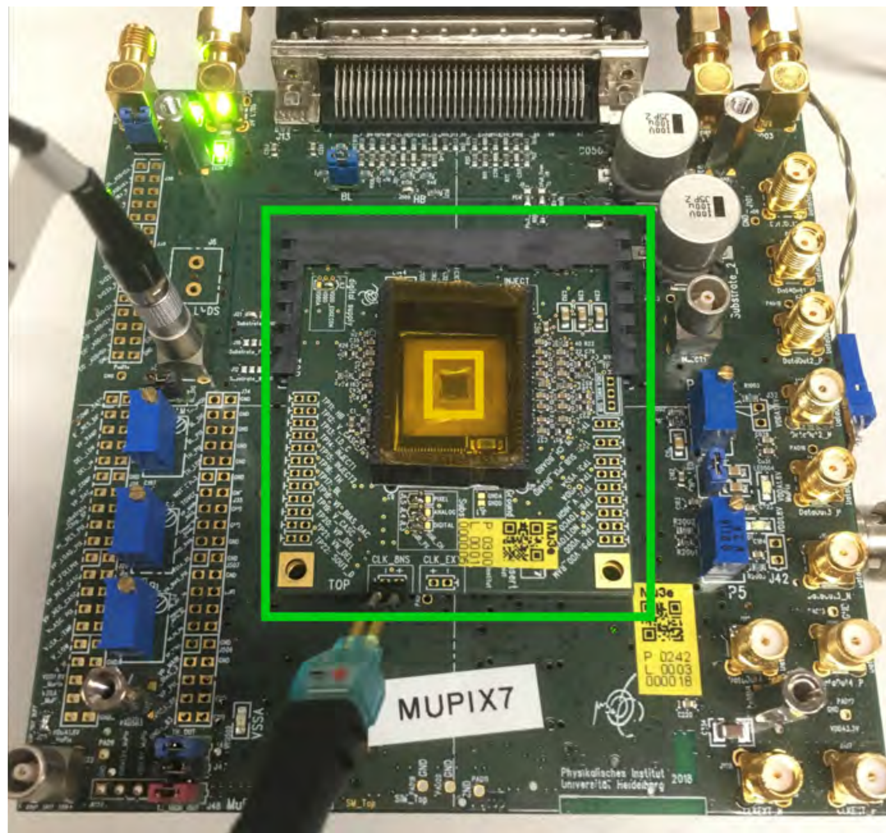

Figure 8.2.: Experimental setup: chip, insert & PCB.

8.2. Timing Reference

To measure the time resolution of MuPix7, a precise timing reference is required. In this setup, it is provided by a scintillating tile read out by Silicon Photo-Multipliers (SiPM) with a pixel pitch of 50 μm.

The used scintillating material is MPPC $S13360 - 3050CS^{®}$ [37] with a sensitive area of $3 \times 3\,mm$.

The tile is placed behind the sensor in order to minimize the influence of severe multiple Coulomb scattering. For the measurements presented later on, a scintillator is operated on a PCB used for the SiPM readout depicted in figure 8.3. The detected signal is also routed to the external FPGA via a SCSI adapter card and read out as described in [38].

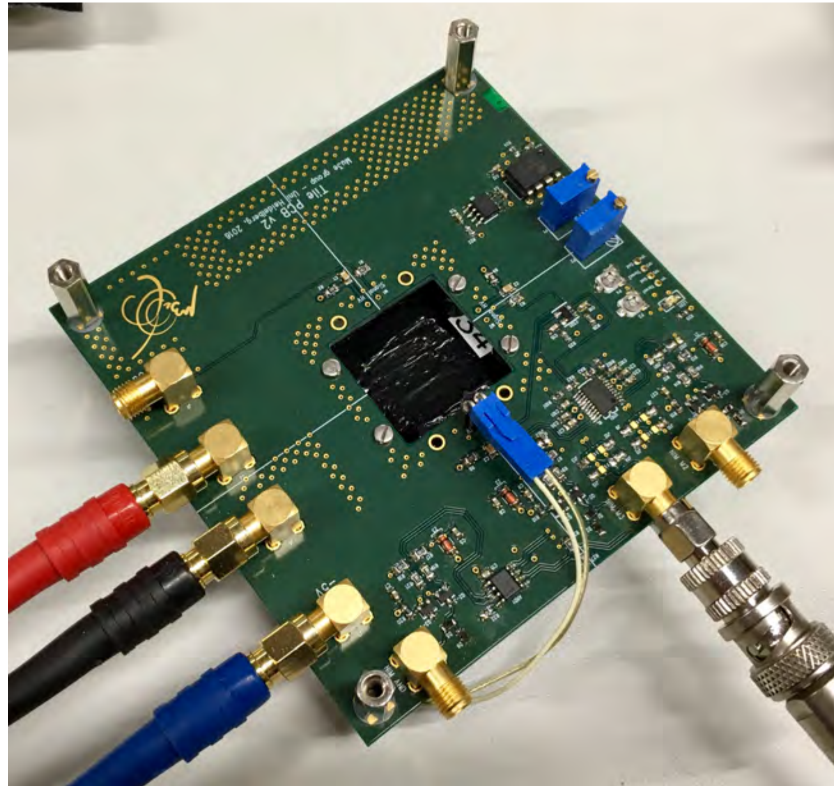

Figure 8.3.: The centered black covered scintillating tile with SiPM is mounted on its PCB.

8.3. Firmware / Software

For data acquisition, a firmware for the FPGA was designed [34] as well as a graphical user interface (GUI) [39].

Once the data is serialized in the state machine, it is routed out to the FPGA via a SCSI connection. As FPGA the commercial available Stratix IV development kit [40] is used and connected via a peripheral component interconnect express (PCIe) to the computer mainboard. A SCSI-III to HSMC control card works as an adapter between FPGA and PCB. The GUI, shown in 8.4, provides control interfaces for various parts of the DAQ and the MuPix7 sensor. Most important for configuring MuPix7 is the window marked with an orange box. Here, most DAC values can be set. A list of standard DACs can be found in tables A1 and A2. In the blue box, the threshold voltage can be adjusted which is externally provided by the mother PCB. For the detailed implementation, see [38]. Furthermore, the GUI provides an online monitoring (purple), status bars (green) and general run control features (red).

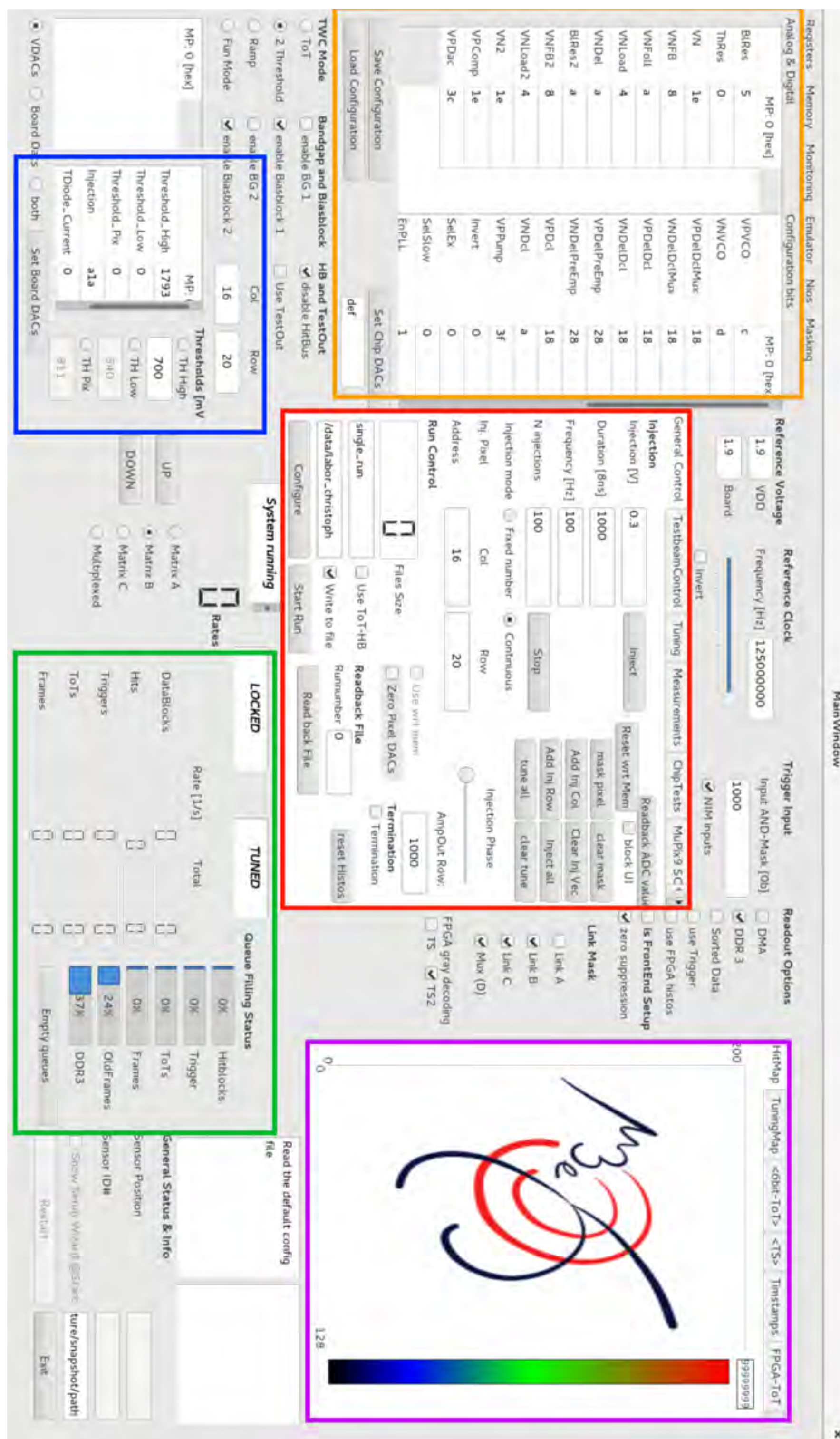

Figure 8.4.: Main window of the single setup GUI with several control panels.

9. Measurement Techniques

For measurements such as the temperature dependence, the time resolution and the signal-to-noise ratio, require external equipment or a certain measurement approach. Depending on the experimental question and the parameters of interest, different measurement techniques are exploited.

9.1. Climate Chamber

In the pulse shape measurement, see section 10.2, the sensor performance is investigated for different environmental temperatures T. To simulate the temperature gradient between $T_{min} = 4°C$ and $T_{max} = 70°C$ [1], a climate chamber was used. The one used for all the measurements, has an inner volume of $402 \times 330\,mm \times 402\,mm$ [41] and a temperature range from $T_{min} = 4°C$ to $T_{max} = 70°C$. For the caböe connections, an additional hole on the upper side is provided. This solution allows for a stable temperature with maximal temperature variations of $\Delta T = 2°C$.

9.2. Radioactive sources

For the measurements, performed within this thesis, two different radioactive isotopes were used, iron-55 and strontium-90.

Iron-55 decays to manganese-55 by electron capture with a half-life time of 2.74 years. The nuclear reaction conserves the electrically neutral charge, but leaves a vacancy in an inner electron shell. This hole is occupied by an electron from an outer shell emitting a photon with the specific energy. The most probable transitions mark the $K_{\alpha,1}$ and $K_{\alpha,2}$ peak with probabilities of 16.2% and 8.2%. The energetic very narrow peaks are treated as a monochromatic line with photon energies $E_\gamma = 5.9\,\text{keV}$.

Strontium-90 emits an $0.55\,\text{MeV}$ electron after β^- decay. With a half-life of 28.79 years, the reaction $n \to p + e^- + \bar{\nu}_e$ produces Yttrium-90. ^{90}Y further undergoes β^- decay into stable Zirconium-90 within a half-life of 64 hours and a decay energy of $E = 2.28\,\text{MeV}$.

9.3. Threshold Scan

For the analysis of threshold scans, the hit digitization procedure is of importance.

The charge collected in a pixel generates an analog charge pulse. For the signal processing and readout, it is digitized by a comparator. This unit compares the hit pulse modulated onto a baseline with an adjustable threshold.

A minimum energy deposited in a pixel is necessary to overcome the threshold. The higher the threshold is set, the smaller is the hit rate and the lower the efficiency because of less high energetic particles. For particles with constant energy, all hits overcome the threshold at the same voltage level. Thus, a step-function from 0 Hz directly to the maximal rate where all pixels fire is expected for the threshold-rate-scan. With the presence of noise, each hit amplitude is lowered or increased and the comparator observes sometimes more, sometimes less hits per time. Thus, a CDF as s-curve like function

$$f(x) = \frac{1}{2}\left(1 + erf\left(\frac{x-\mu}{\sqrt{2\sigma^2}}\right)\right) \tag{9.0}$$

can be fitted to the data as shown in figure 11.4. The error bars are not visible behind the data points. The mean value μ gives the signal amplitude plus the baseline voltage and the standard deviation σ the noise which is the reason for the smoothed step-function. Because of the stimulation with an injection signal, the number of pulses are known. Therefore, it can be interpreted as a Bernoulli experiment which converges against a binomial distribution for a large data set. Hence, the function is equal to a cumulative distribution function. With the assumption that for a large data set n the measured value k is approximately the expected value μ, sigma is

$$\sigma = \sqrt{np(1-p)} \approx \sqrt{k(1-k/n)} \tag{9.0}$$

where $p = k/n$ is the probability of success. Here, a success means the observation of a crossing particle.

9.4. Time-over-Threshold

The pulse amplitude is the integrated charge deposited in a pixel. During digitization, the pulse amplitude is assigned to the time-over-threshold (ToT) information. The duration the hit pulse exceeds the threshold is called ToT, see figure 9.1. Thus, the amplitude is indirectly measured via the ToT technique.

Because of electronic noise, the ToT varies even for a monoenergetic injection voltage. Therefore, all ToT measurements are performed a thousand times and the mean value and the standard deviation are taken.

The digital comparator output for a single pixel, the hitbus, can be directly read out through a test-point situated on the insert. Here, the ToT is the time period

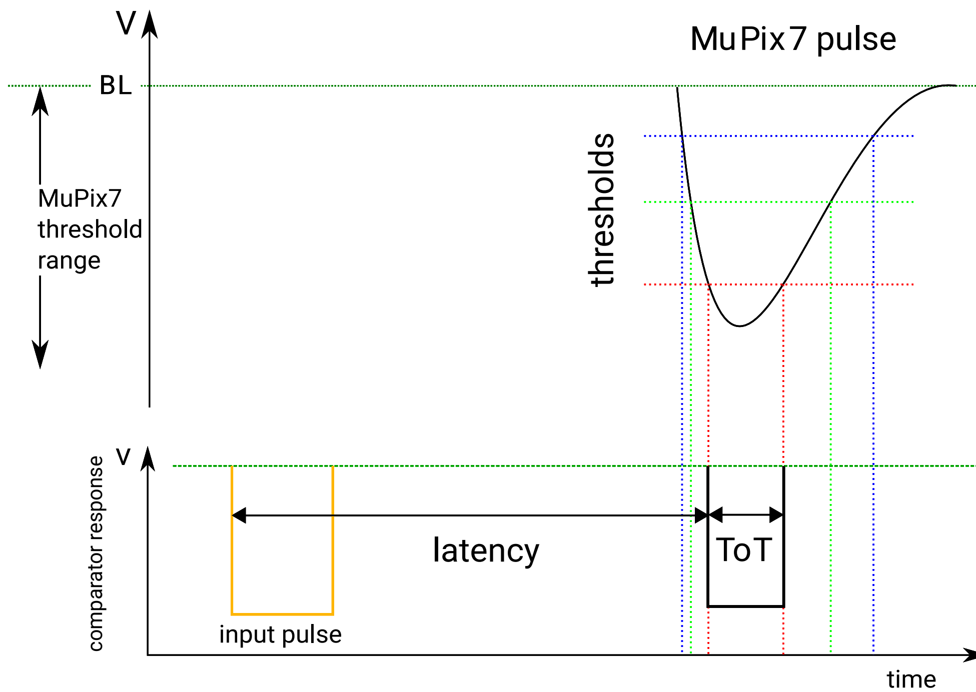

Figure 9.1.: Sketch to show the ToT measurement done within the comparator [28].

between a rising and falling edge of a digital pulse.

Although the analog pulse is not accessible in MuPix7, the ToT gives a possibility to reproduce the analog pulse.

For the MuPix7 sensor, the ToT is a time-under-threshold (TuT) as the amplifier inverts the charge pulse.

Part III.

Measurements

10. Commissioning of the Setup and the TSI chip

The setup for the currently characterized MuPix8 was adjusted for the already studied MuPix7 to compare the MuPix7 prototypes produced by AMS and TSI. A particular insert was designed for the usage with MuPix7 on the MuPix8 v2 PCB and the data acquisition software had to be adjusted. For the commissioning of the setup, previous measurements, performed in [33, 28, 38], are revised with a dedicated MuPix7 PCB and the previous version of the GUI discussed in [28].

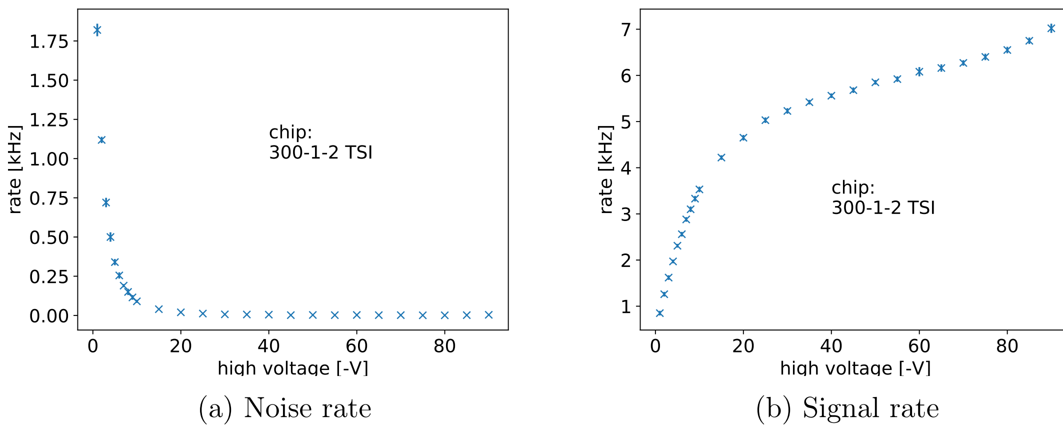

(a) Noise rate

(b) Signal rate

Figure 10.1.: The noise (a) and signal (b) behavior for a reversely biased diode is measured with the new setup.

In order to test the setup, the diode characteristics for an increasing high voltage is measured. Applying high voltage to the diode in reverse bias mode increases the width of the depletion zone as explained in equation 4.1. Because particle interactions are only registered in the depletion zone, the hit rate is proportional the detection volume which increases for a higher voltage. The measurement result, showing the current as function of the applied voltage in figure 10.1a, is consistent with the expectation. However, figure 10.1b shows a second increase after saturation because of electron showers occurring near the diode's breakdown voltage.

The noise rate is inversely correlated with the high voltage because of the decreasing capacity which can be seen in figure 10.1b. For the assumption that the overall conductivity is determined by the diodes conductivity in equation 4.1, it is proportional to the inverse square root of the high voltage.

After the successful configuration and readout of the chip, the data transmission and voltage behavior are consistent with previous measurements presented in [33].

10.1. Temperature dependence

Sensor temperatures from $T = 4°C$ to $T = 70°C$ are expected in the Mu3e detector [1]. As a transistor's performance dependents on the temperature, previous measurements with AMS sensors [28] showed a temperature dependence of the signal pulse shape.

The pulse shape is reconstructed out of a threshold scan in temperature steps of $\Delta T = 20°C$. At each threshold, two points in time are noted corresponding to both threshold crossings within the comparator. As explained in section 11.2, the first timestamp has some threshold dependent delay, called latency, whereas the second timestamp is the sum of the latency plus the ToT (described in section 9). The measurement results for TSI prototypes are plotted in figure 10.2. The corresponding measurement with an AMS produced chip was conducted with the old setup shown in figure 10.3. Adjustable PCB parameters as the comparator baseline were adapted from the previous setting, but do not allow for a quantitative comparison.

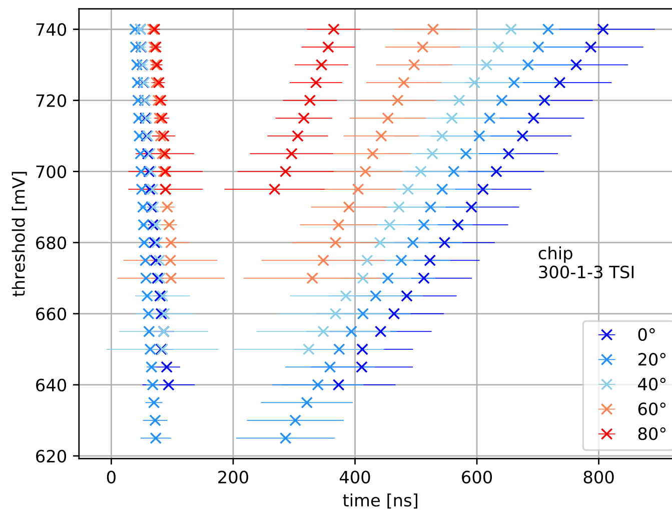

Figure 10.2.: Temperature dependent pulse shape measurements with the new setup and a TSI chip

The leading edges rise nearly at the same time with similar delay for increasing temperatures. However, the falling edge as well as the peak are influenced by the temperatures. The ToT decreases non-linear for increasing temperatures, indicating a temperature dependent signal processing. For a constant temperature increase, the pulse differences become bigger at high temperatures.

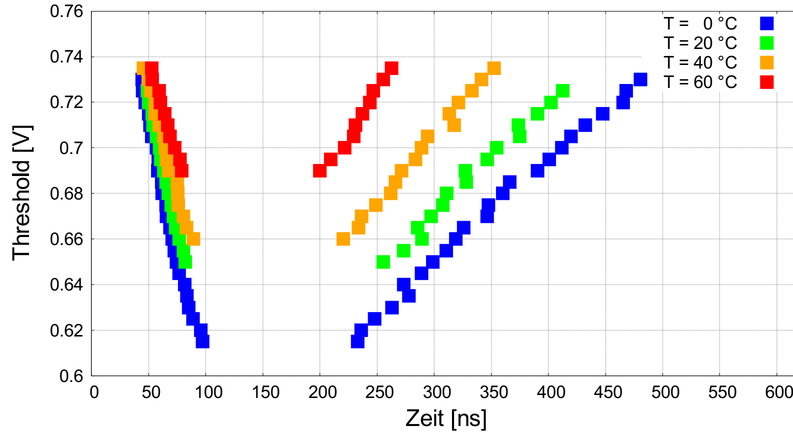

Figure 10.3.: Old pulse shape measurement with the AMS MuPix7 setup taken from [28]

Comparing the new and the old measurement, performed in [28], a similar behavior is observed, illustrated in figure 7.2, where the temperature dependency was ascribed to BLResPix2.

The temperature measurements have shown that TSI sensors behave similar to AMS chips.

10.2. Injection gauging

For comparability of ToT measurements, discussed in section 9, the injected charge is expressed by number of electrons. The ToT-histogram of an injection voltage is gauged to that of an ^{55}Fe source.

However, the ToT is not sampled on the MuPix7. Nevertheless, it is possible to get the required information for a single pixel via the hitbus, accessible through a test-point provided on the insert.

ToT distributions of an injection voltage (blue histogram) and ^{55}Fe (orange) are shown in figure 10.4. For a specific injection voltage, the ToT forms a Gaussian distribution due to thermal noise. The ^{55}Fe histogram shows a similar widened peak with the same underlying Gaussian,fitted in red, with its mean value μ_{gaus}. ^{55}Fe data also show a divergent tail to lower values. This is caused by the photoelectric electron loosing part of their energy outside the active pixel area or in neighboring pixels. Then, one hit with lower energy or two separated hits are registered. The tail distorts the total mean value μ_{Fe} and has to be excluded for fitting a suitable injection current to the ^{55}Fe source. An injection voltage of $V = 0.42$V equivalent to an ^{55}Fe source was determined.

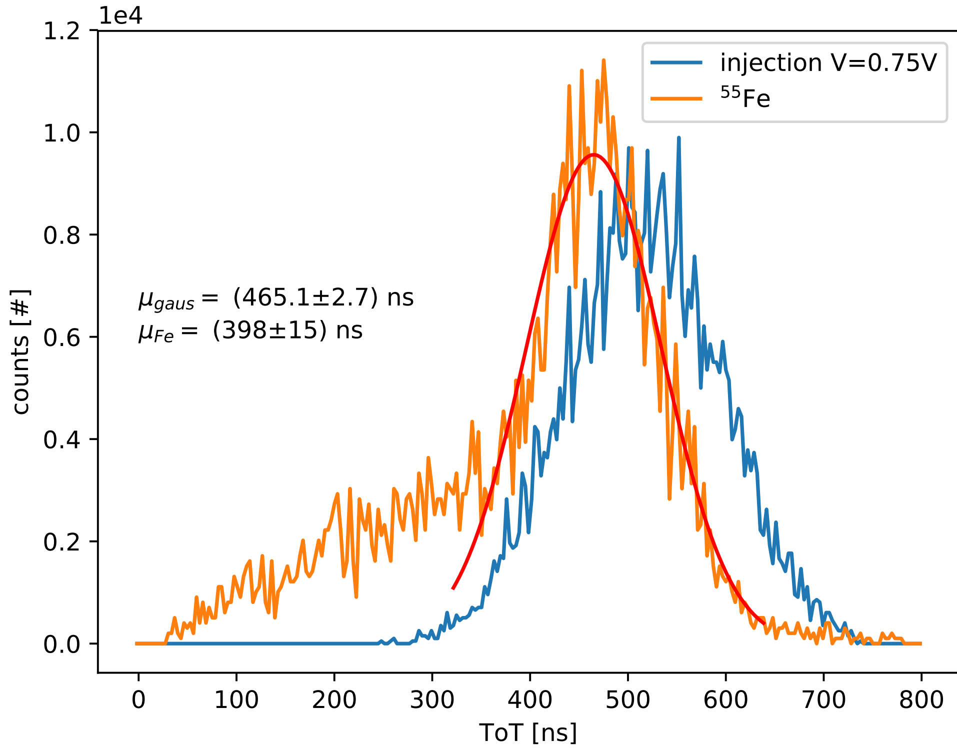

Figure 10.4.: ToT spectra of an injection with $V = 0.75\,V$ (blue) and of an ^{55}Fe source (red).

The number of electrons for the iron source N_e can be derived through the energy of an emitted photon divided by the energy necessary for producing an electron-hole pair in the diode (see 4.1).

$$N_e = \frac{E_\gamma}{E_{ep}} \tag{10.4}$$

With $N_e = 1617$ for the ^{55}Fe source, the diode capacitance $C_{inj} = 0.64\,\mathrm{fF}$ was calculated with equation 10.4. It is independent on the signal source and can be used to determine the electrons for different injection voltages V_{inj} with the same formula. The following plots show the injection voltage as well as the corresponding number of electrons:

$$N_e = \frac{C_{inj} V_{inj}}{e} \tag{10.4}$$

11. Direct Comparison: AMS vs. TSI

The well-characterized MuPix7 sensor were initially produced in the AMS $H18$ process [7] which is no longer supported. Thus, a similar high voltage process by TSI Semiconductor [8] is investigated. Both are based on the same IBM process.

MuPix7 sensors produced by AMS and TSI are studied in measurements, presented in [28], [42] and [33]. Beside the same setup parameters, multiple sensors from both foundries are tested for a direct comparison.

Some parameters, such as efficiency, are only measurable in a testbeam campaign as described in [35]. Several important components of the sensor are investigated with the laboratory setup, starting with the diode, the signal processing electronic and the state machine.

11.1. Diode

In the diode, a particle interaction generates electron-hole pairs. With an electric field big enough, these electrons trigger secondary electrons which indicates the breakdown voltage. A higher breakdown voltage allows the operation at higher voltages which improves the efficiency due to the larger expected depletion zone described in section 4. The electric field strength is strongly affected by the manufacturing procedure. Thus, it is a suitable indicator for a comparison of AMS and TSI.

Current measurements in appendix A1 have shown that with a fully connected test-board not only the diode's leakage current is observed, but also that of the surrounding electronics. With connected power- and data cables, the overall leakage current is about two orders of magnitude higher than the current flowing between all diode n-wells and p-substrates. To bypass the readout electronics, the diode's leakage current can be accessed through a test-point on the insert PCB. Also, the measurement was performed in darkness because ambient light affects the measured leakage current.

The leakage currents are measured in the region around the diode's breakdown voltage shown in figure 11.1. Due to the exponential increase of the leakage current, a linear function can be fitted to the right hand side of the I-V-curve, in a logarithmic plot. The left hand side is just a constant current, The intersection between both fits quantifies the breakdown voltage. Therewith, the average breakdown voltages result in $U_{AMS} = (92.89 \pm 0.18)\,V$ for AMS and $U_{TSI} = (95.92 \pm 0.12)\,V$ for TSI.

Statistical fluctuations can be seen for each production process, but they are too small to explain the observed deviation.

Although a significant difference was shown, these results do not affect the used standard settings. The high voltage of $-85\,\mathrm{V}$, used for previous MuPix7

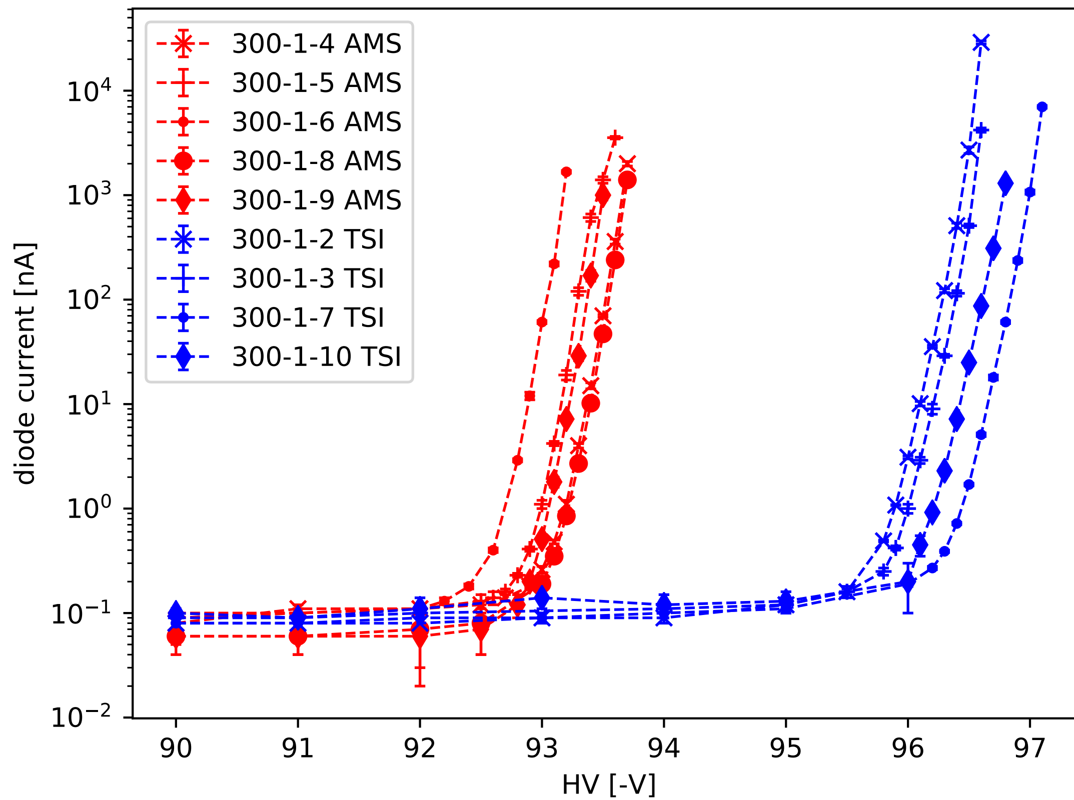

Figure 11.1.: I-V-curve around the breakdown voltages for AMS (red) and TSI (blue) prototypes.

measurements, is far enough from the breakdown region independent of the foundry.

An increase of the breakdown voltage can be achieved by redesigning the pn-junction as shown in [43].

11.2. Signal amplification

In order to investigate the amplification circuit, the signal amplification of different injection voltages is measured. In order to mimik different charge depositions, various voltages are injected instead of using radioactive sources. This is a good method to evaluate the voltage dependent signal shaping in the electronics.

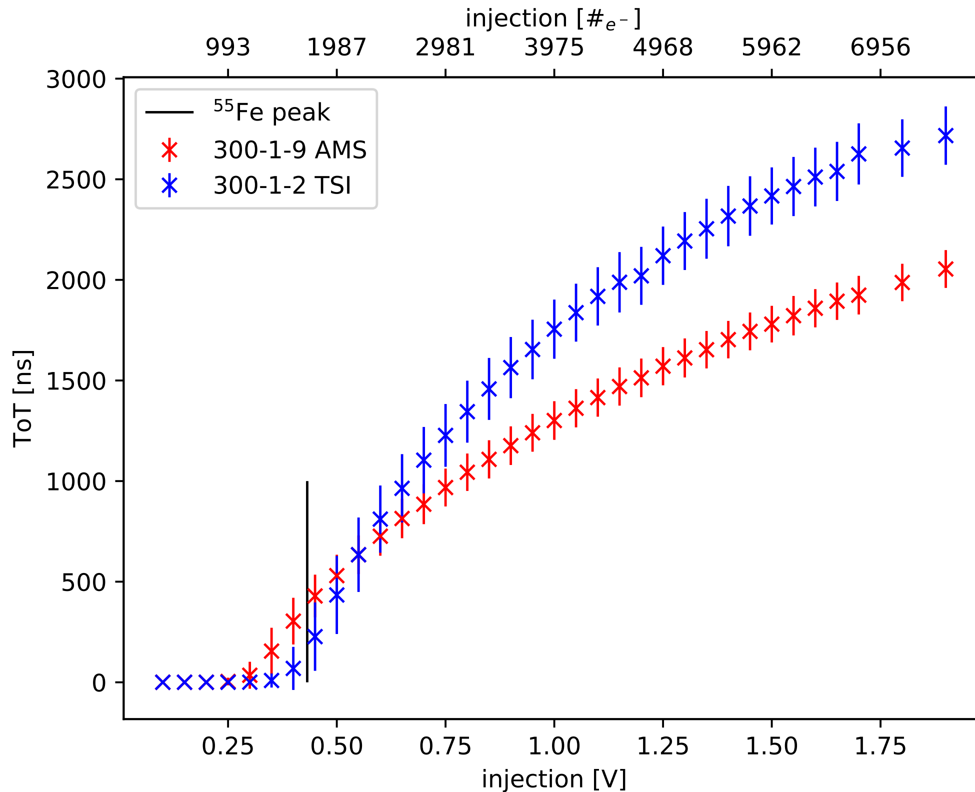

Figure 11.2.: Measured ToT as function of the injection voltage also given in numbers of electrons at a threshold of 700 mV.

A linear relation would indicate no dependence between the signal processing and the initial charge deposition. Instead, figure 11.2 shows a clear change of the gradient of the ToT. For larger pulse heights, a change in the injection voltage has a smaller influence on the ToT.

The calibration with the iron source for both sensors is done within the amplifiers operating range where a linear behavior can be assumed.

Because of the discrepancy between AMS and TSI, the region around the ^{55}Fe peak between $V = 0.2\,V$ and $V = 0.7\,V$ is studied in more detail with all available sensors. The mean ToT for both foundries does not show significant differences anymore.

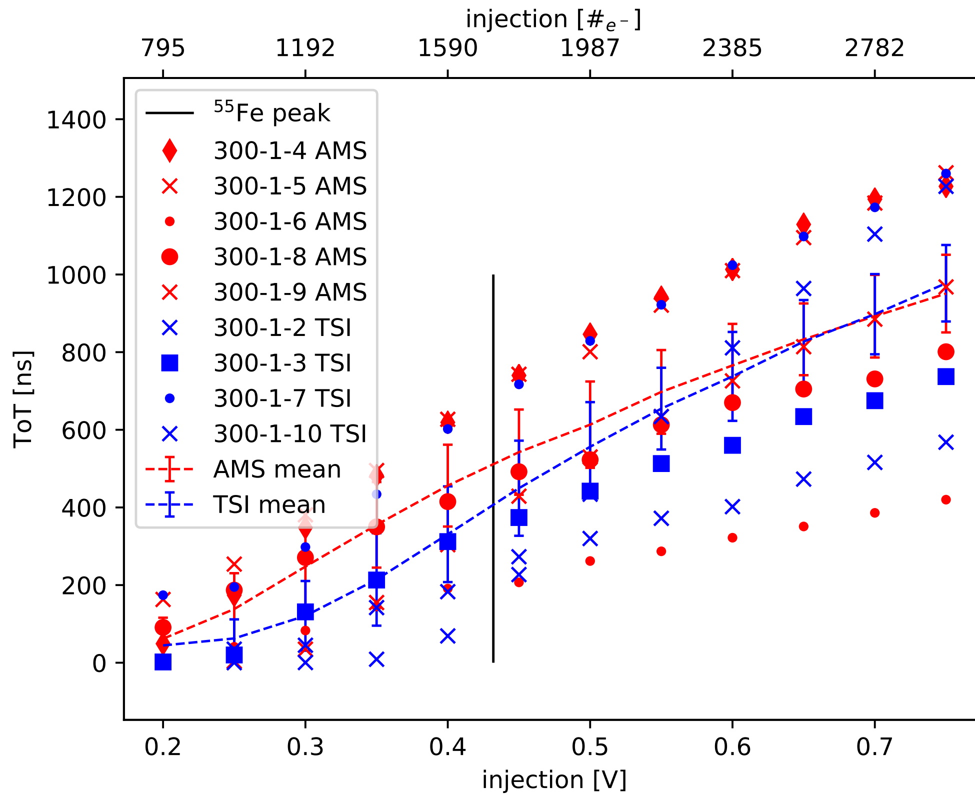

Figure 11.3.: Measured ToT as function of the injection voltage also given in numbers of electrons at a threshold of 700 mV.

The deviation in the lower range might be affected by differing thresholds and an asynchronous increase of the ToT. Therefore, the firstly measured discrepancy was just a chip-to-chip fluctuation and any adjustments of the setup parameters are not necessary.

For further measurements an injection voltage of $0.75\,V$ is used where AMS and TSI chips behave similar.

11.3. SNR measurement

The signal-to-noise ratio (SNR) for a sensor quantifies the performance of the signal processing emphasizing the hit signal which corresponds to a crossing particle.

For calculation, the average hit signal of crossing particles and the mean noise level are required. Noise can disturb a hit signal by thermal noise during the generation of a signal hit as well as in the digital readout. Also additional noise hits

can be induced by hits in neighboring pixels or in a diode by thermal excitation.

Because of a pixel-to-pixel varying threshold, a simple addition of every pixels threshold scan is misleading. The threshold is scanned against the hit rate and analyzed for each pixel individually described in section 9.

There are two methods computing the SNR with differing results which are both determined in figure 11.7. Out of all s-curve fits to the pixels, a histogram with all mean values and standard deviations was drawn, shown in figure 11.5. The error can be calculated according to the propagation of uncertainty. The SNR can be calculated according to the following formula with the baseline $b = 0.8\,\mathrm{V}$ and the average mean $\bar{\mu}$ and the mean standard deviation $\bar{\sigma}$ of all single pixel cumulative distribution functions (CDF, function 9.0):

$$SNR_{\mu} = \frac{|\bar{\mu} - b|}{\bar{\sigma}} \tag{11.3}$$

A second possibility is the direct calculation of an SNR value for each pixel individually. Then, the averaged values in equation 11.3 are the fit parameters of each pixel's CDF. To obtain an overall parameter SNR_{Σ}, the mean of a Gaussian of the pixel SNR values in histogram 11.6 is determined.

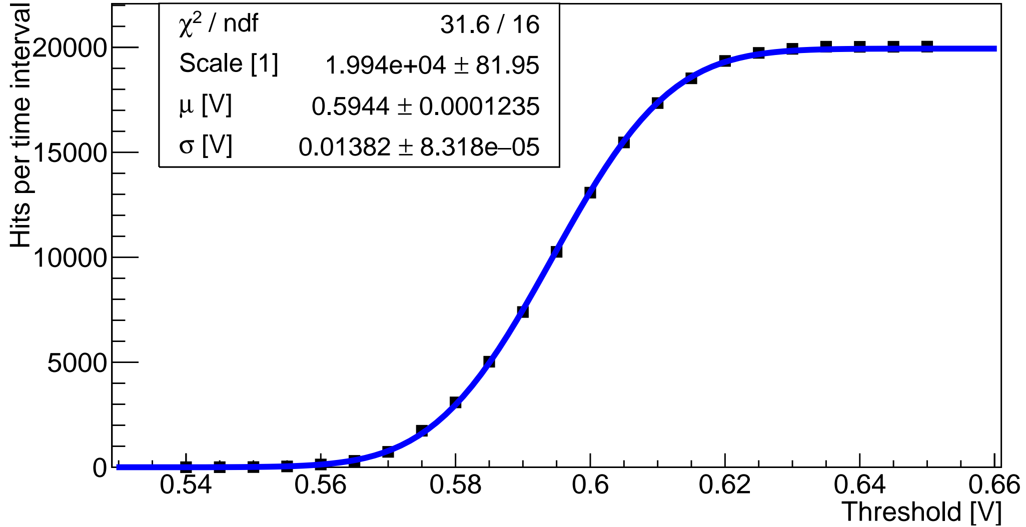

Figure 11.4.: Threshold scan with fitted s-curve function for pixel (5/4) of sensor 300-1-2.

For each data point 20000 injection pulses with an amplitude of 0.4 V equivalent to an ^{55}Fe source were applied with a frequency of 1000 Hz and a duration of 800 ns.

The SNR values for AMS are slightly higher than for TSI sensors indicating

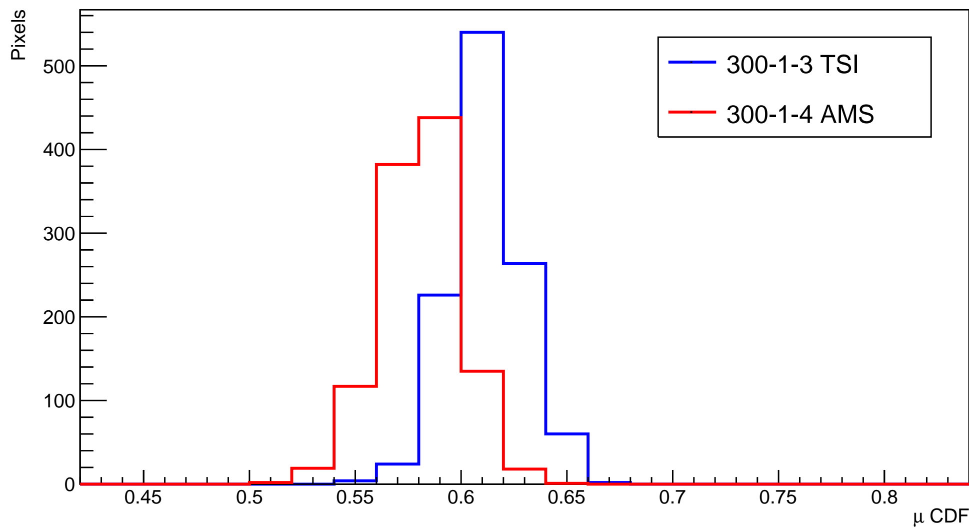

Figure 11.5.: Pixel-to-pixel distributions of the s-curve mean.

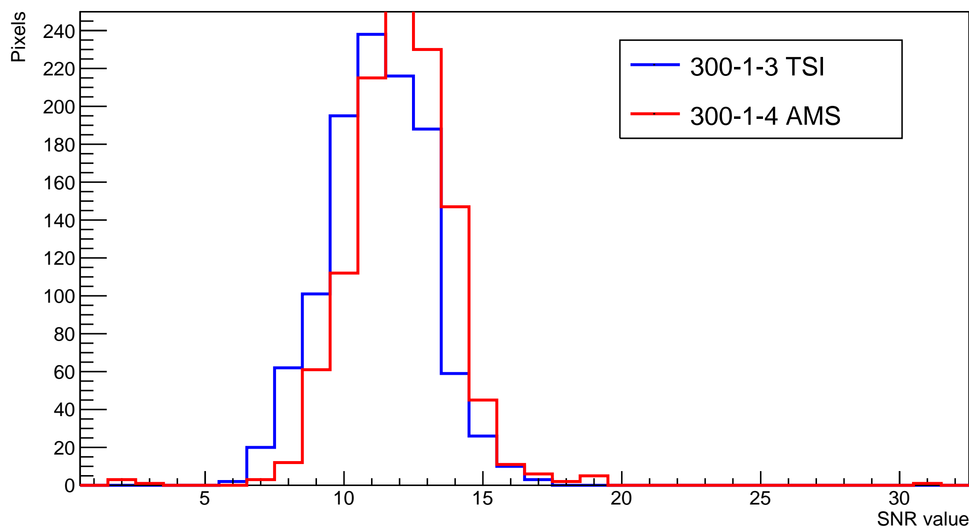

Figure 11.6.: SNR value histogramed for every pixel of one sensor.

a better signal transmission. Figure A3 shows the average mean and standard deviation for both foundries and a difference in the mean can be seen. The origin of the noise is not further studied here, but can be looked up in [44]. Figure 11.3 depicts statistical variations, but no significant differences between AMS and TSI.

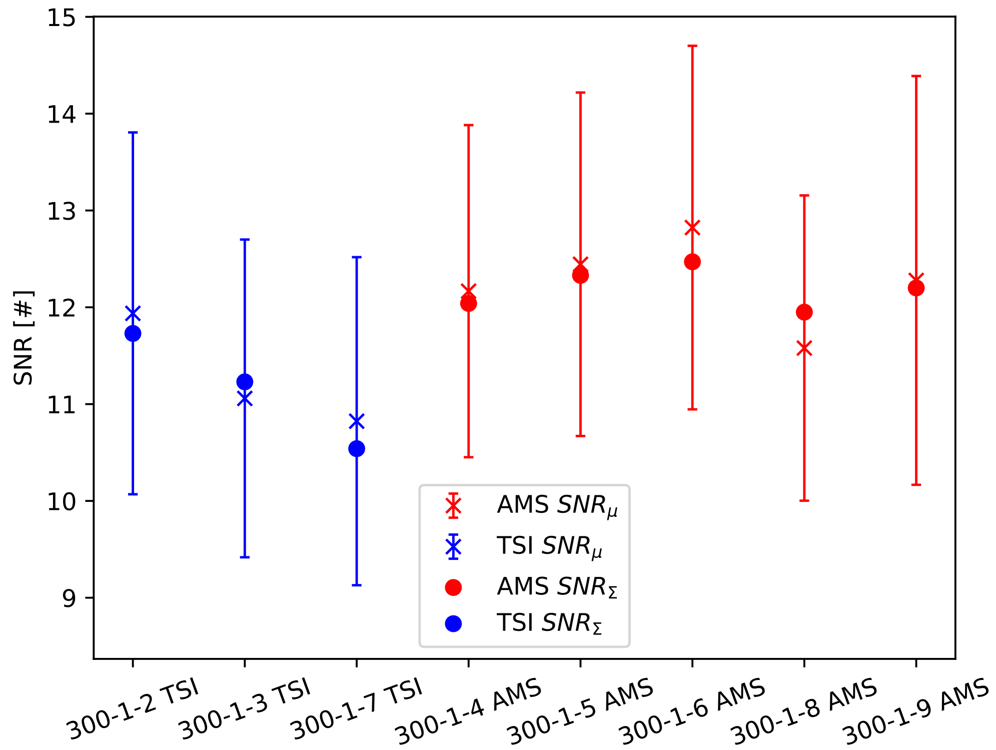

Figure 11.7.: Both determined SNR values for all DUTs taking all pixels into account.

The mean SNR values for both foundries are:

$$SNR_{\mu,TSI} = 11.3 \pm 1.7$$
$$SNR_{\mu,AMS} = 12.3 \pm 1.8$$

Due to lots of pixel-to-pixel fluctuations, high uncertainties are measured. The measured difference of the mean is withinn one standard deviation. However, the measurement should be repeated with the tuning feature implemented which equalizes the thresholds for a more consistent SNR measurement.

11.4. Characterization of the PLL

The stability of the clock is crucial for the correct operation of the chip. The general functionality of the PLL is described in section 7 where the DAC settings are explained among others. In order to characterize the stability of the PLL, the jitter is investigated, describing the deviation of the on-chip clock compared to a stable reference clock. In figure 11.8, the stable reference signal in red is triggered on the oscilloscope [45] as well as the on-chip signal in green shown in order to quantify the variations. The rising and falling edges of the on-chip clock within the blue box are plotted in the orange histogram. The jitter is determined as the standard deviation σ of the Gaussian histogram described by equation 11.7.

$$f(x) = \exp\Big(-\frac{(x-\mu)^2}{2\sigma^2}\Big) \tag{11.7}$$

This is exactly generated with an adjustable reference clock frequency of 125 MHz. The clock signal with half the frequency of the reference signal can directly be accessed through a test-point on the PCB seen in 8.2. Due to statistical fluctuations caused by thermal noise a Gaussian distribution is expected.

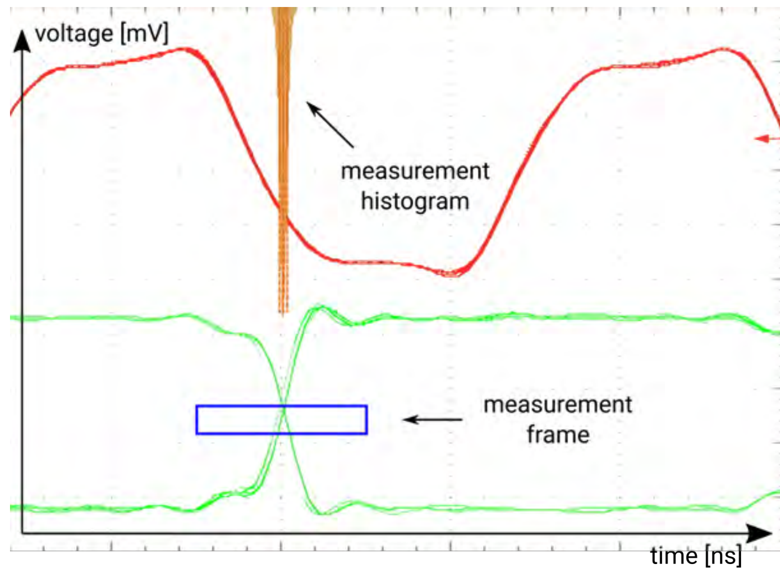

Figure 11.8.: Jitter of the on-chip signal and reference clock are investigated over time on an oscilloscope [45] with different voltage amplitudes.

For the following measurements, all DACs are set to default values as listed in table A2 apart from the scanned value.

Figure 11.9 displays the jitter depending on the VPVCO values, measured from

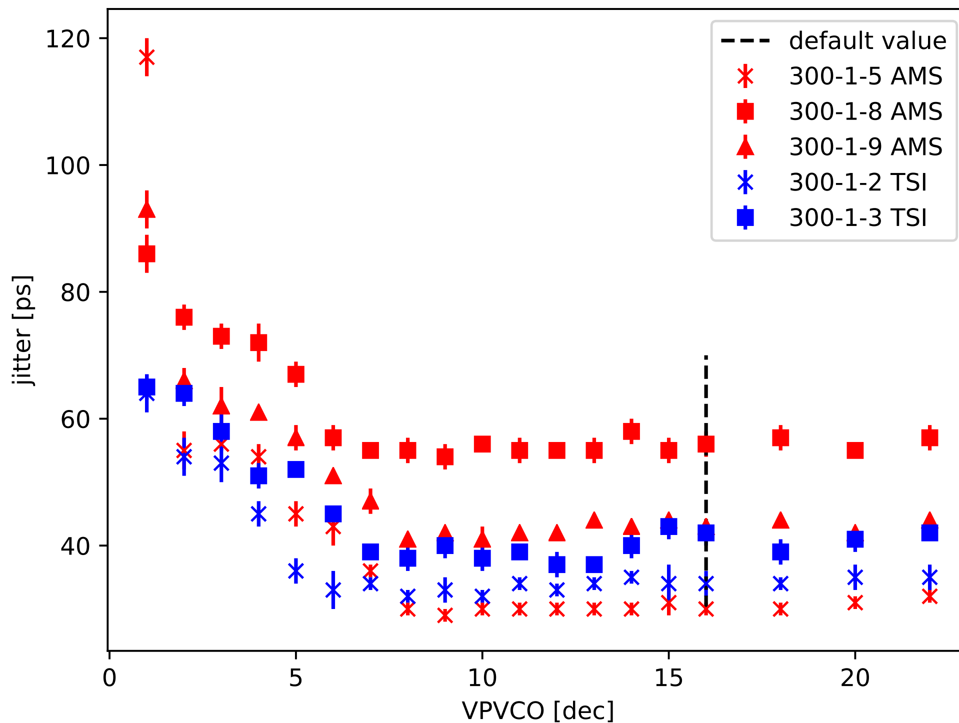

Figure 11.9.: Measured jitter as function of VPVCO controlling the positive VCO potential.

0 to 22. According to a 6 bit DAC, the possible range covers $0 - 63$. The jitter is stable within the uncertainties for VPVCO larger than 8. A steep increase of jitter is observed for smaller DAC values. This behavior seems to be stronger for the AMS chips as for the TSI ones. At higher DAC values, the jitter is constant with statistical fluctuations. Nevertheless, less jitter conveys for the TSI chips. However, the overall shape is the same. This means that the default DAC value does not need to be changed. A lowering of the VPVCO value would lower the power consumption, but negative effects on other chip parameters are not investigated.

The DAC value applied to the charge pump controlling TOVCO is called VNVCO. The scanned DAC value range does not show any effects on the jitter, but an overall lower jitter for TSI chips (see figure 11.11).

VPPump controls the feedback performance by adjusting TOVCO, illustrated in figure 7.3. Figure 11.10 shows a similar dependency between the scanned DAC values and the corresponding jitter as the VPVCO scan 11.9. It can be seen that

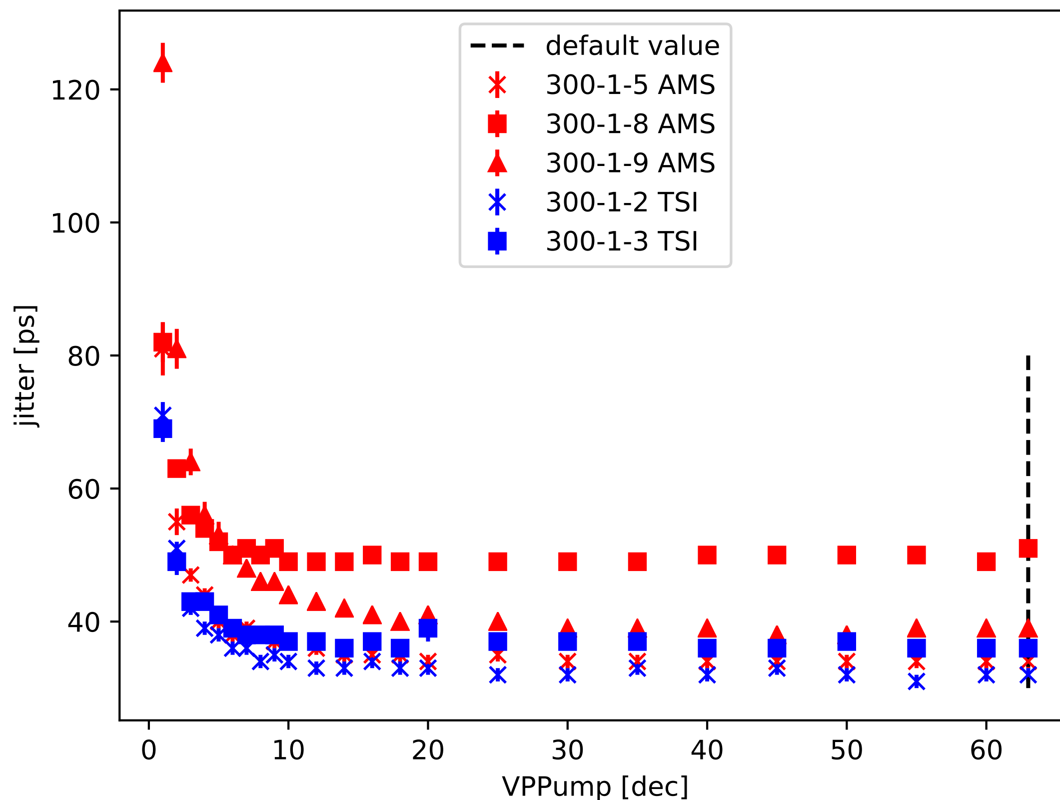

Figure 11.10.: Measured jitter depending on VPPump controlling the feedback via TOVCO.

the jitter depending on VPPump is not as fluctuating as for the previous scanned VPVCO value. Again, there is no significant difference between AMS and TSI produced chips which is the comparison of interest although the jitter seems to be slightly higher for the AMS sensors.

Here, the chosen standard DAC value is the highest possible. Due to a negligible power consumption of VNVCO, an adjustment is not necessary. Also the adjustment of this parameter for TSI sensors is not necessary.

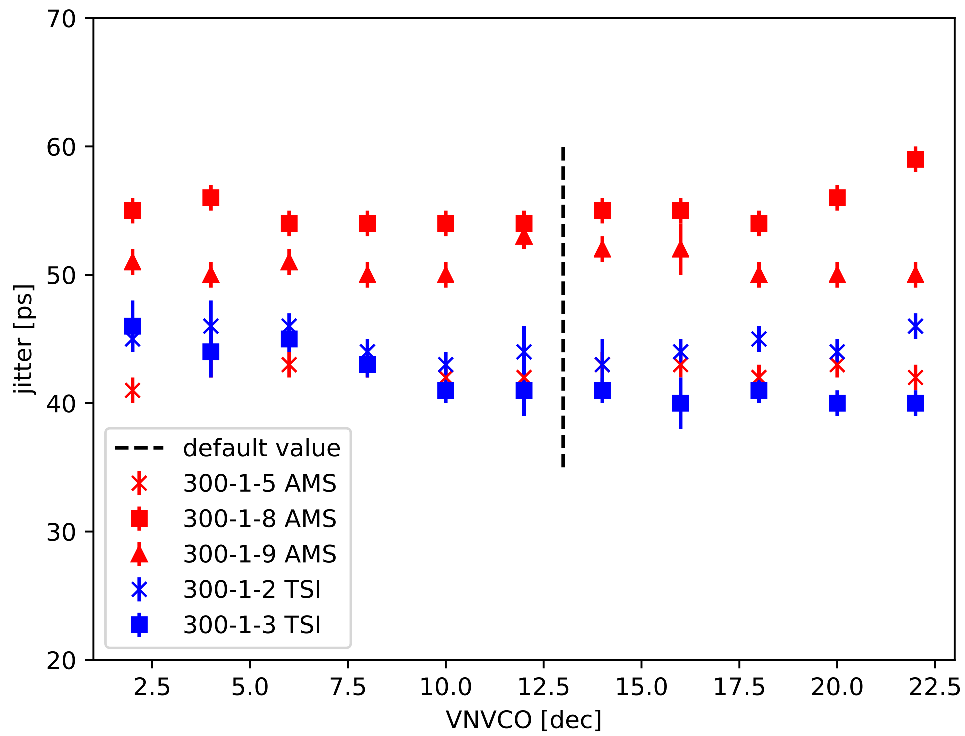

Figure 11.11.: Measured jitter as function of DAC VNVCO controlling the bias TOVCO.

11.5. Time Resolution

For high luminosity experiments, a good time resolution is needed [46]. Therefore, the important parameter is determined for the MuPix7 prototypes.

To obtain the resolution, the hit timestamp is correlated with a reference time information of the same particle given by a scintillating tile. The latency distribution, hit timestamps (TS) minus reference timestamps, is calculated and plotted in a histogram. Due to limited temporal resolution caused by delay and time-walk, the dominant peak is smeared out as a Gaussian distribution. Because of random background matches, the distribution also has an underlying triangular shape for random coincidences. To take care of this effect, the fit function

$$f(x) = c_1 \cdot \exp \frac{(x-\mu)^2}{\sqrt{2}\sigma} + c_2 \cdot (c_3 - |x|) \tag{11.11}$$

has an additional term which is not visible in small scale around the peak. In this equation, the constants $c_{1,2,3}$ are fit parameters. The parameter of interest is the standard deviation σ of the Gaussian distribution given in $2\,ns$ timestamp bins. The other fit parameter, the mean value μ, represents the mean delay of the hit timestamp regarding the trigger timestamp.

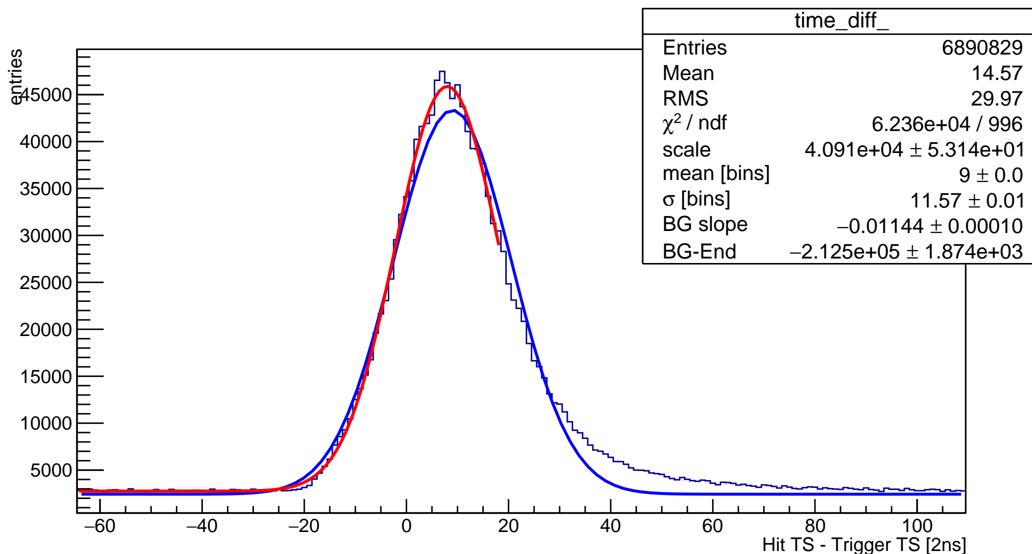

Figure 11.12.: Function 11.11 fitted to the Histogram of the difference of $HitTS - TriggerTS$ for two fit ranges.

The fit in figure 11.12 shows a slight difference depending on the fit range. The time resolutions for a single measurement do not differ significantly by ±1.5 ns. A

tail to the peaks right-hand side disturbs the Gaussian distribution. The histogram is asymmetric due to time-walk as illustrated in figure 9.1. Depending on the pulse height and hence its ToT, the delay is larger for smaller signals. A detailed investigation of the time-walk and possible corrections can be found in [38] for MuPix8.

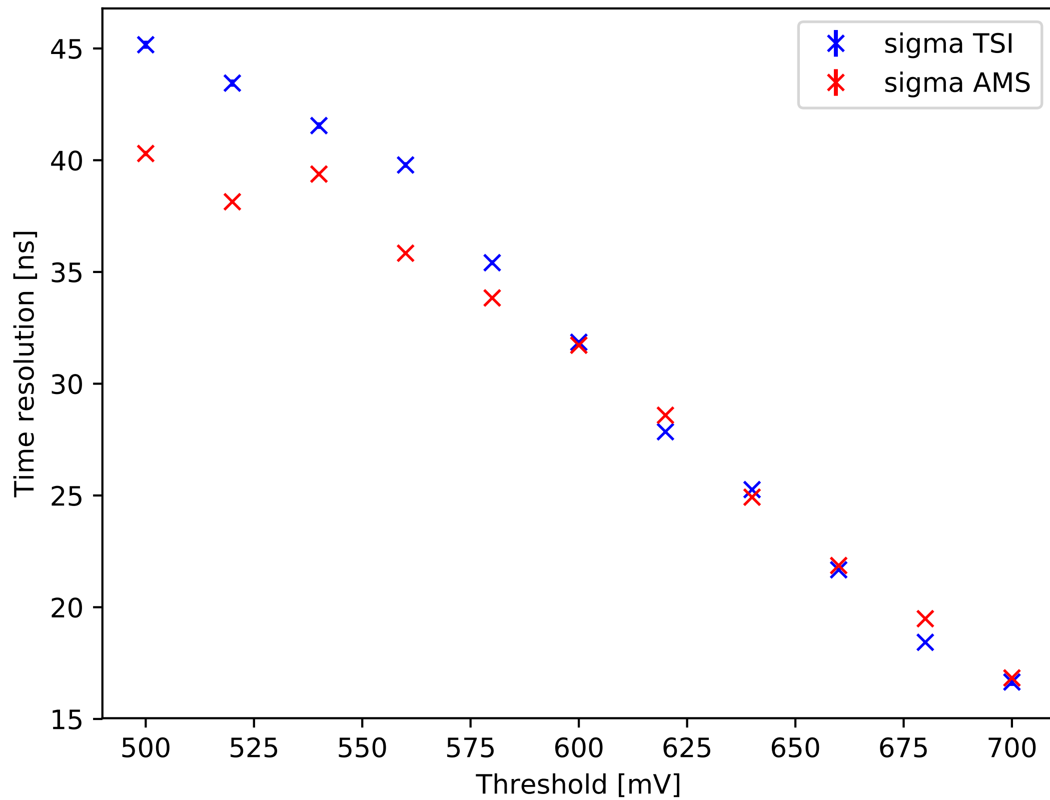

Figure 11.13.: A threshold scan at $HV = -70\,V$ and baseline $b = 0.8\,\mathrm{V}$ was performed for an AMS and TSI sensor.

The threshold scan plotted in 11.13 shows that the higher the threshold the better the time resolution. In fact, a higher threshold means a value closer to the baseline, hence, a lower comparator level. For all results, an HV of $-70\,\mathrm{V}$ was applied to each pixel. For thresholds higher than $700\,mV$, the registered data is dominated by noise. That's why the time resolution cannot be precisely measured anymore. Therefore, $680\,mV$ seems to be the best compromise of a good time resolution with enough distance to the noise.

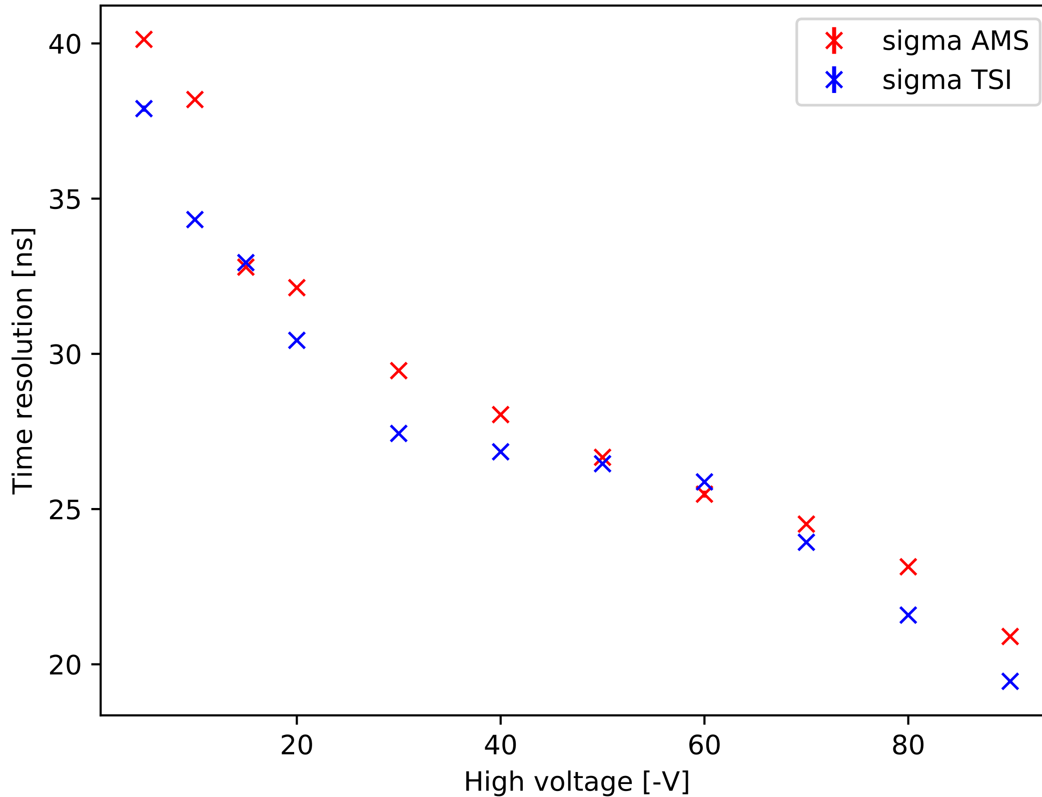

Figure 11.14.: At a threshold of 680 mV and baseline $b = 0.8\,\mathrm{V}$ the time resolution depending on the voltage was measured.

A scan of the applied high voltage in figure 11.14 shows an improved time resolution for higher values as expected. Because of an newly adjusted setup, the time resolution measurements depending on the voltage and the threshold show differing results for comparable settings.

However, a comparison between an AMS and a TSI chip do not show significant differences. The statistical fluctuations within each scan are of the same order.

In figure 11.15, each data point was taken at a threshold of $680\,mV$ and HV= $-85V$. According to the previous measurements, these values are a good choice for a comparison. The sigma parameter of the Gaussian fit from each sensor in figure 11.15 is the time resolution as explained before. Here, all TSI produced sensors perform up to 1.5 ns worse than the available AMS ones. The mean time resolution for AMS is $\mu_{AMS} = (22.3 \pm 0.6)\,ns$ while the TSI one is $\mu_{TSI} = (23.7 \pm 0.7)\,ns$

which is significant.

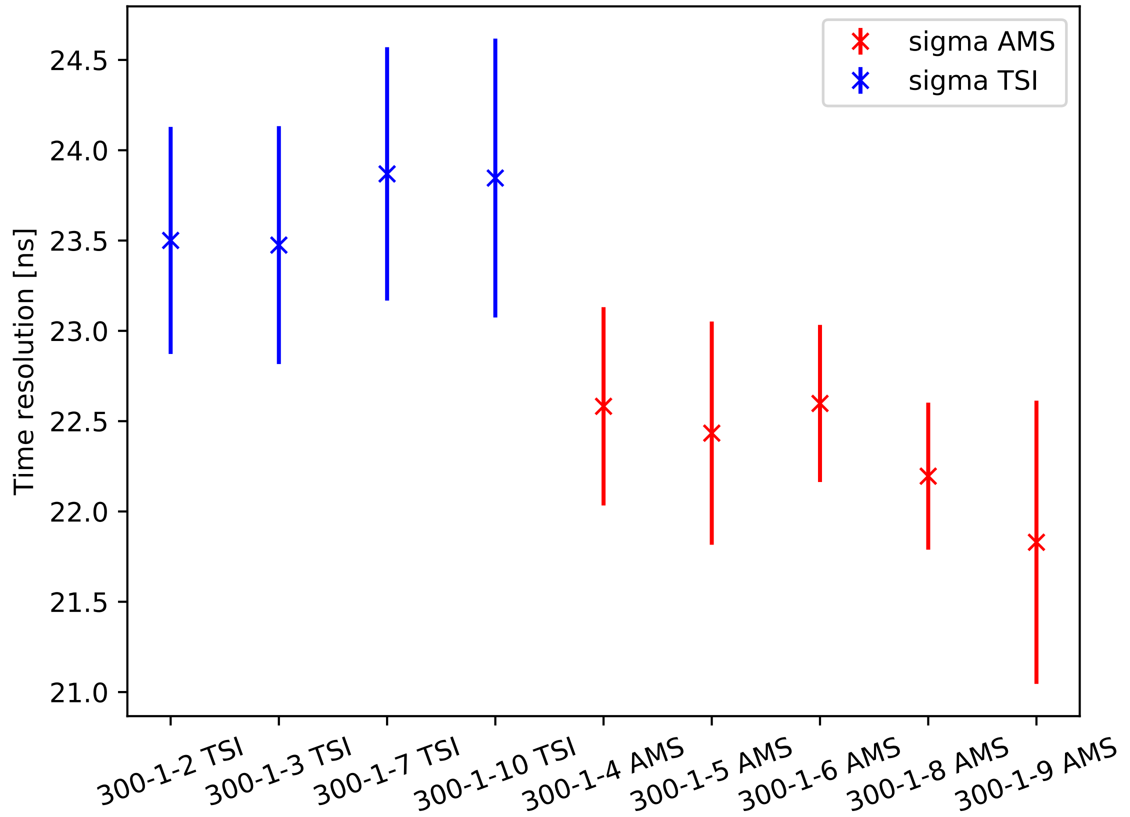

Figure 11.15.: Time resolutions measured at HV= $-85\,\mathrm{V}$ and a threshold of $640\,\mathrm{mV}$.

With ToT information 11.2 for each hit, the time resolution can be further improved according to [38]. For the next generation sensor, MuPix8, the ToT is provided for every pixel. Thus, an algorithm for time-walk correction is implemented and can further improve the time resolution as shown in this thesis [38].

11.6. Power Consumption

The power consumption of a sensor can give an indication if components might behave different. A higher power consumption means increased heat dissipation in the circuitry which effects the performance of the sensor (see figure 10.2) or can even damage the chip. That is why the final detector will have a cooling system ensuring low temperature over the entire experiment. Following the detector design [1], a maximum cooling power of $400\,W/cm^2$ is specified.

The $5\,V$ low voltage applied to the PCB is split up into three different voltages provided by on-board voltage converters. The power consumed by the pixel cells itself is called VDDA and VSSA respectively whereas VDD powers the digital logic and the state machine. For detailed investigations, these voltages can be applied individually and hence the currents can be measured separately for each supply voltage. For the MuPix7 setup, the voltages are as follows: VDD = $1.8\,V$, VDDA = $1.8\,V$ and VSSA = $1.5\,V$.

The power consumptions, plotted in figure 11.16, show a significant difference between AMS and TSI sensors. The consumed power as well as the relative discrepancy is the largest for VDD, but a difference can also be seen for the other voltages. For VDD the power consumption for the tested TSI chip is about 25% higher than for the AMS one, for VDDA and VSSA the TSI chips still consume about 15% more power.

The overall power consumption for each foundry accounts for:

$$P_{TSI} = (129.3 \pm 1.0)\,mW$$
$$P_{AMS} = (105.3 \pm 4.1)\,mW$$

For an enlargement of the sensor, the poewr consumption of the pixel matrix scales with the sensor size as well as the digital periphery. The state machine and thus, parts of VDD stay constant at a bigger pixel matrix because this unit is only required once per chip. Thus, a bigger sensor will consume less power per area. A further investigation will determine if the difference will also decrease.

Also the distribution of each sensor's power consumption within one foundry is noteworthy. The AMS chips vary much more than the measured TSI chips. It proves the previous assumption that the TSI production might have lower chip-to-chip variations.

For a more detailed study, each sensor component can be turned on separately and thus, the power consumption of each component can be accessed with the corresponding DAC value. As VDD shows the highest discrepancy and the highest

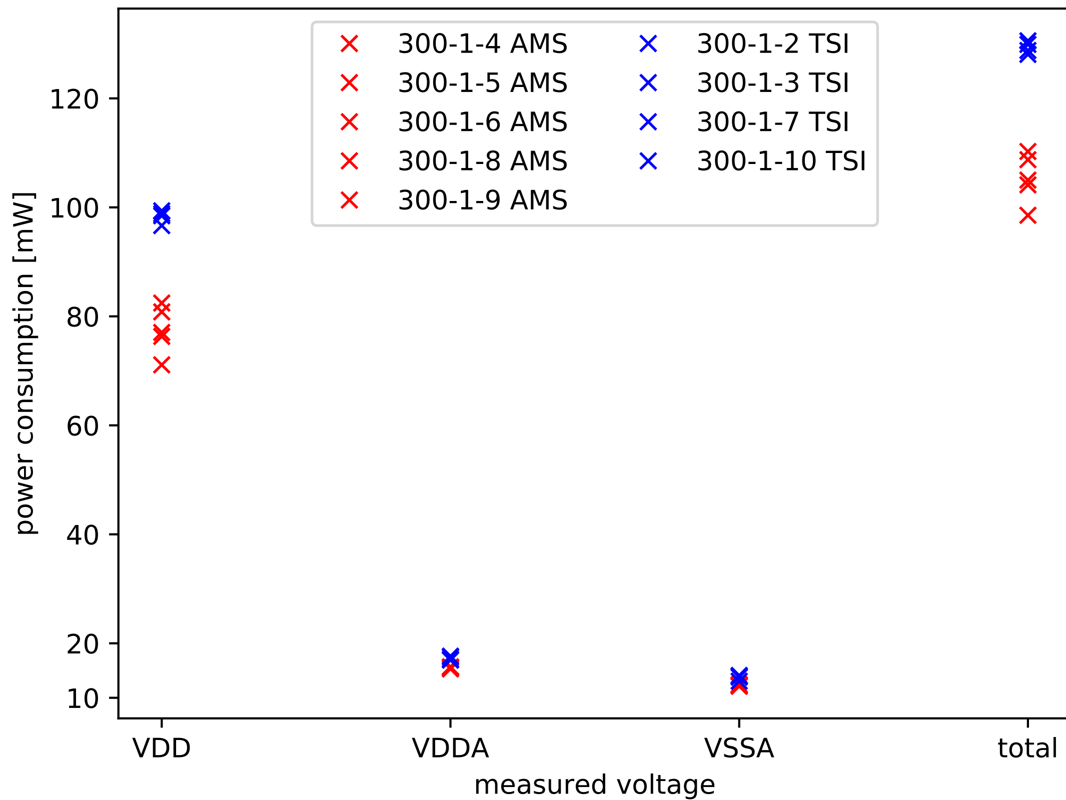

Figure 11.16.: Measured power consumption for every supplied low voltage and the total power consumption for all available sensors.

amount in total, $VDDA$ and $VSSA$ are not further studied. The DAC values for VDD shown in table 11.1 control the main power consuming parts of the chip, see also table A1. Other DACs also contribute to the power difference, but are negligible.

11.7. LVDS Readout

Regarding the relative current differences of each current between the investigated foundries, the DAC VNLVDS displays the highest discrepancy between TSI and AMS. This huge difference in the power consumption of VDD is investigated in detail.

In order to analyze the effect of the DAC value, the LVDS readout signal is

DAC	current (TSI) [mA]	current (AMS) [mA]	TSI/AMS
VN2	4.4	3.9	1.13
VNLVDS	19.1	8.0	2.39
VPComp	4.4	3.8	1.16
VPDac	12.4	11.5	1.08

Table 11.1.: Power consumption per components controlled by certain DAC in the digital readout.

analyzed with a high resolution spectrum analyzer. The DAC VNLVDS itself adjusts the 'eye height'. Further dependencies could not be observed during the measurements. The other 'eye' parameters such as the width were not significantly affected by VNLVDS shown in figure A4.

In figure 11.18, the 'eye height' is compared to the power consumption for every DAC value. At the same DAC value the data points show a different 'eye height' of up to 400% between TSI and AMS sensors.

For a TSI chip , the same power consumption as for an AMS one can be reached by decreasing the DAC value. The higher 'eye height' for TSI chips results in a better readout signal quality. Hence, it gives a better readout performance of the sensor. On the other hand, a higher 'eye height' requires more power to create the LVDS signal. A lower value of VNLVDS= 2 for TSI chips results in the same 'eye height' of AMS sensors for VNLVDS= 14.

The power consumption by VNLVDS is independent of the chip area. Therefore, the additional amount of power will decrease for a larger sensor.

To find the optimum ratio between the 'eye height' and power consumption, this ratio is shown in figure 11.18. It shows a local maximum at the default DAC value where the TSI chip is by 35.4% more efficient than the AMS chip. Thus, the DAC VNLVDS does not have to be changed.

11.8. Global Bias Current

To understand the difference in the LVDS eye height, two global bias voltages powering LVDS are investigated.

A test-point situated on the insert (light green rectangle in figure 8.2) is used to access the voltages VPBiasDAC and VCASC. VPBiasDAC powers most parts of the chip as the global bias voltage. Due to the voltage measurement in series to the circuitry, an operation during the measurement was not possible.

Figure 11.19 for VPBiasDAC and figure A5 for VCASC only show slight discrep-

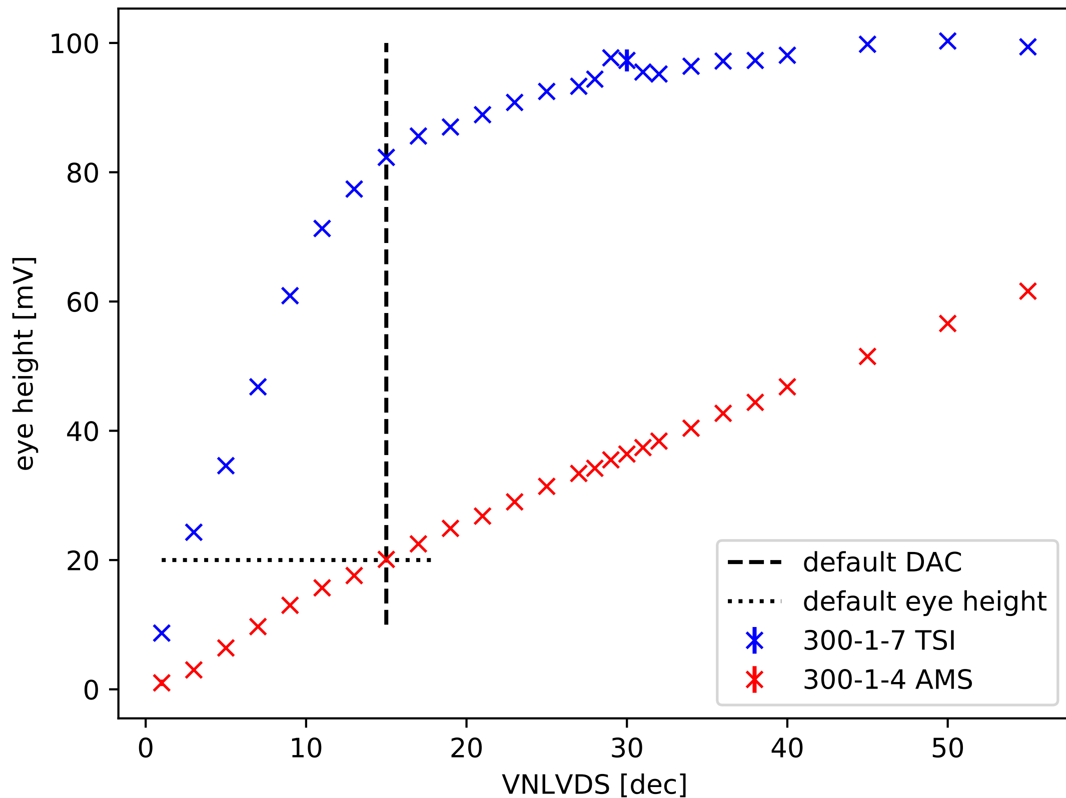

Figure 11.17.: The 'eye height' is measured for a TSI and an AMS chip depending on the DAC VNLVDS.

ancies between both foundries of just a few mV. But these minor variations can result in the different 'eye heights' seen in figure 11.18 through shifted working points.

The different voltages are also present in figure 11.20 where the resistivity is studied for every tested sensor. Hence, a current can be measured at constant VDD = 1.8 V according to Ohm's law. The chip was operated as usual and the current could be measured at test-points on the insert PCB.

The ratios voltage over current for TSI chips differ widely. Hence, a huge statistical fluctuation might affect the responsible transistors. However, for all AMS sensors similar value were measured. The congruent behavior shows that AMS' production seems to be more precise.

In general, the fluctuation of the resistivity for VPBiasDAC is about four times

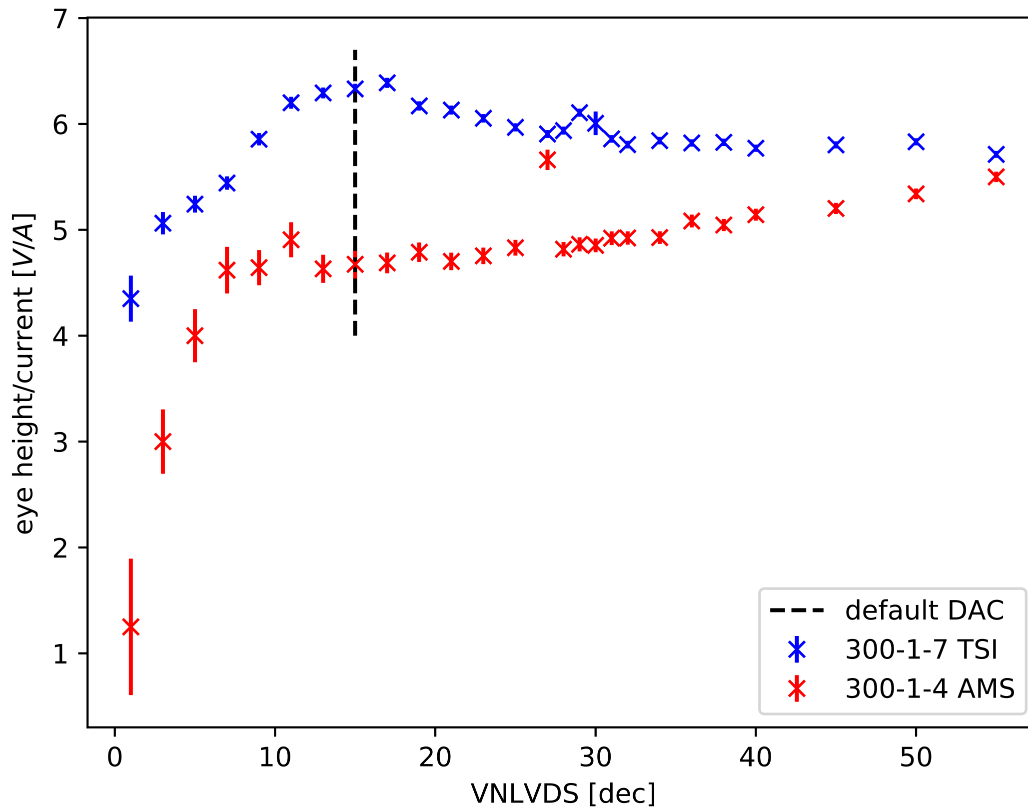

Figure 11.18.: The ratio 'eye height' over power consumption is measured for a TSI and an AMS prototype.

greater than for VCASC. Therefore, the variations of AMS are not that severe than the TSI ones. For future MuPix generations, an investigation of the LVDS and other parts connected to the measured global bias currents is useful.

Due to the global currents observed at these test-points, the differences might also affect several other components of the sensor. However, the difference between the sum over all measured powers for single DAC values and the overall consumption is not significant. Therefore, no difference aside statistical fluctuations in other areas are expected.

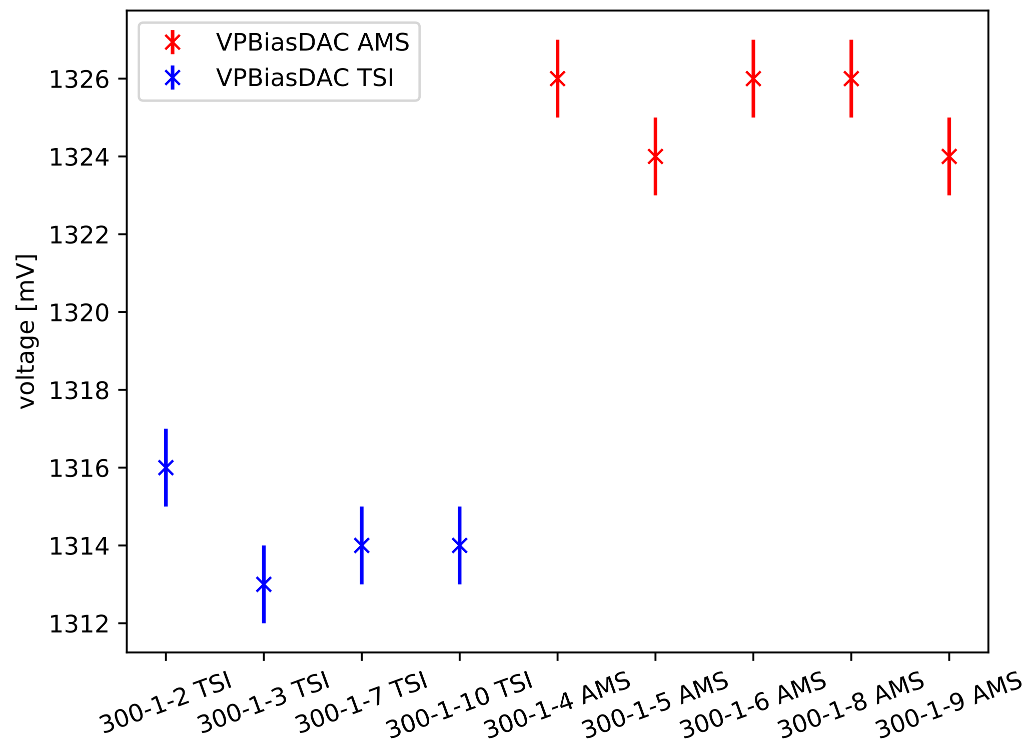

Figure 11.19.: Global voltage working points powering the LVDS signal creation.

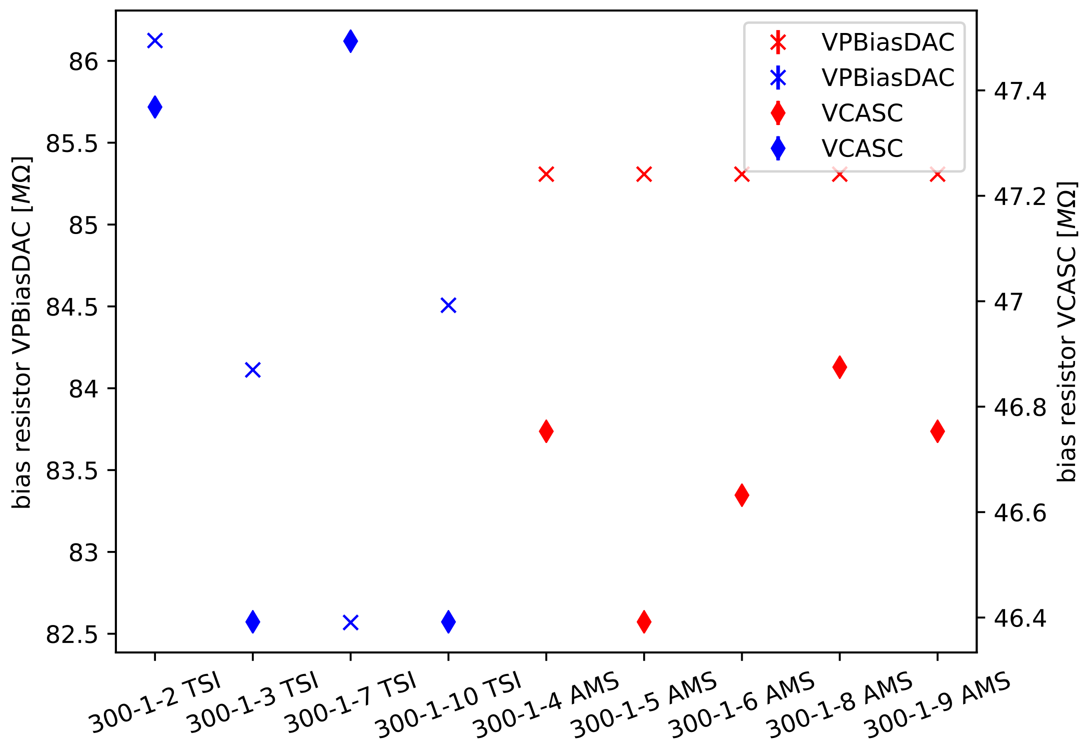

Figure 11.20.: Global bias resistivity measured for VPBiasDAC and VCASC.

Part IV.

Discussion & Outlook

12. Summary & Discussion

For the comparison of an HV-MAPS prototype, produced by two different foundries, the default setup for MuPix8 was successfully adapted and commissioned. The most important sensor parts of MuPix7, namely the diode, the amplifier and the clock circuitry were compared between the old AMS H18 and the TSI High-Voltage process. Together with important performance observables such as the time resolution and the power consumption, the qualification, performed in this thesis, gives a broad overview.

Within the reversely biased diode, the breakdown voltage is determined to $HV = -96\,V$ for the TSI chips and to $HV = -93\,V$ for the AMS ones.

The performance of the amplification circuitry has been measured with an injection voltage, after gauging to an ^{55}Fe source for comparability.. Except statistical variations between the sensors, the results do not differ significantly.

The PLL was investigated as part of the readout state-machine. All TSI chips perform with a mean jitter of the on-chip clock of $\mu_{TSI} = (35.0 \pm 1.1)$ ps contrary to $\mu_{AMS} = (42.0 \pm 0.8)$ ps. TSI sensors perform significantly better. However, chips from both processes fulfill the requirements of a jitter smaller than 100 ps according to [47].

Comparing the time resolution between AMS and TSI sensors with $\mu_{TSI} = (23.7 \pm 0.7)$ ns and $\mu_{AMS} = (22.3 \pm 0.6)$ ns, a difference was measured. Nevertheless, the overall measured time resolutions do not differ significantly.

The power consumption shows the highest discrepancy between AMS and TSI using the same configuration with $P_{AMS} \approx 105\,mW$ and $P_{TSI} \approx 129\,mW$. The significant difference is mostly caused by VDD with $\Delta P_{VDD} \approx 7.5$ mW, powering the periphery and the state machine.

The LVDS analysis clearly shows that the TSI sensors have larger ‘eye heights’ at the same power consumption, indicating an improved signal quality for TSI chips.

The difference can be explained with slightly differing bias currents of the LVDS signal.

To summarize, AMS and TSI chips do not differ significantly in most tested performance parameters measured with the same settings. An optimization of the sensor configuration for TSI sensors is possible for the power consumption of the LVDS readout. Therefore, the production can be transferred to the TSI high voltage process with the default configuration in most components.

13. Outlook

In the laboratory measurements can not determine all performance parameters of an HV-MAPS. One of the most important parameters for a sensor is its efficiency concerning particle detection. Previous measurements of AMS sensors show values above 99% [39] with optimized settings. This parameter still needs to be measured for TSI chips. A high energetic particle beam is required to cross a telescope with multiple sensor layers allowing for precise track reconstruction.

Another feature not available for this thesis is the threshold tuning. Each pixel has a 4 bit tune DAC (TDAC) to adjust its threshold value within the comparator. Thus, differing single pixel behaviors can be compensated which leads to a uniform noise response, described in [39].

Important for long-term operation in a particle detector is the performance under irradiation. To study the radiation hardness, chips can be irradiated with high doses to simulate the radiation damage in particle collider experiments. AMS chips were fully functional after neutron irradiation with $5 \cdot 10^{15}\,\mathrm{n_{eq}/cm^2}$, but showed a lower efficiency level according to [39]. The same measurements are of interest to qualify the radiation hardness of TSI produced sensors.

Part V.

Appendix

Voltage	Circuit	Function	Effect
VN2	Amp2	Current Source	steers current
VNLoad2	Amp2	Voltage divider	adjusts amplification
VNFB2	Amp2	Resistance	linear CSA feedback
VPComp	Comparator	Current source	Current & speed control
BL	Comparator	Baseline	Voltage offset for signal & Comparator input
THR	Comparator	Threshold	Comparator reference
BLRes	Comparator	Restoration	Shaping
VPDAC	Comparator		Tuning
VNDel	Edge detector		Delay

Table A1.: Summary of the bias voltages of the digital part [33].

DAC	Default	Effect
VPVCO	16	oscillator bias
VNVCO	13	phase locked loop bias
VPPUMP	63	charge pump bias
VPDCL	24	global DCL bias
VNDCL	16	global DCL bias
VPDelDCL	40	delay for DCL clock
VNDelDCL	40	delay for DCL clock
VPDelDCLMux	24	delay for DCL mux clock
VNDelDCLMux	24	delay for DCL mux clock
VNLVDS	24	strength of LVDS buffer
VNLVDSDel	0	strength of pre-emphasis buffer
VPDelPreEmp	24	delay of pre-emphasis
VNDelPreEmp	24	delay of pre-emphasis

Table A2.: Default chip DAC setting optimized by Sebastian Dittmeier [34].

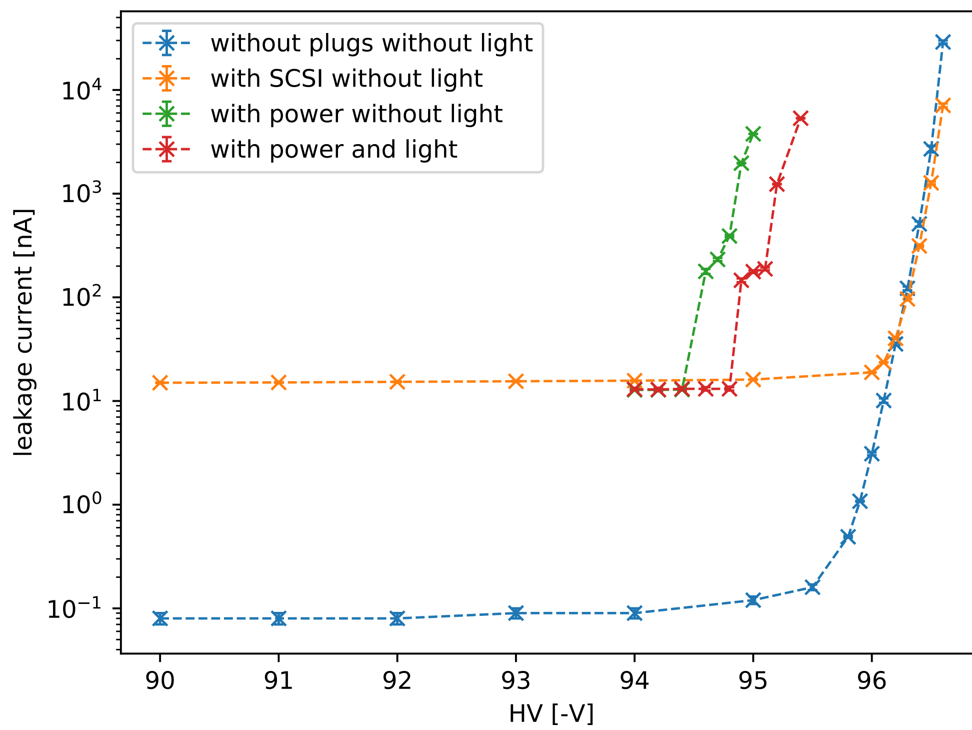

Figure A1.: I-V-curves are measured with and without connected cables and light irradiation.

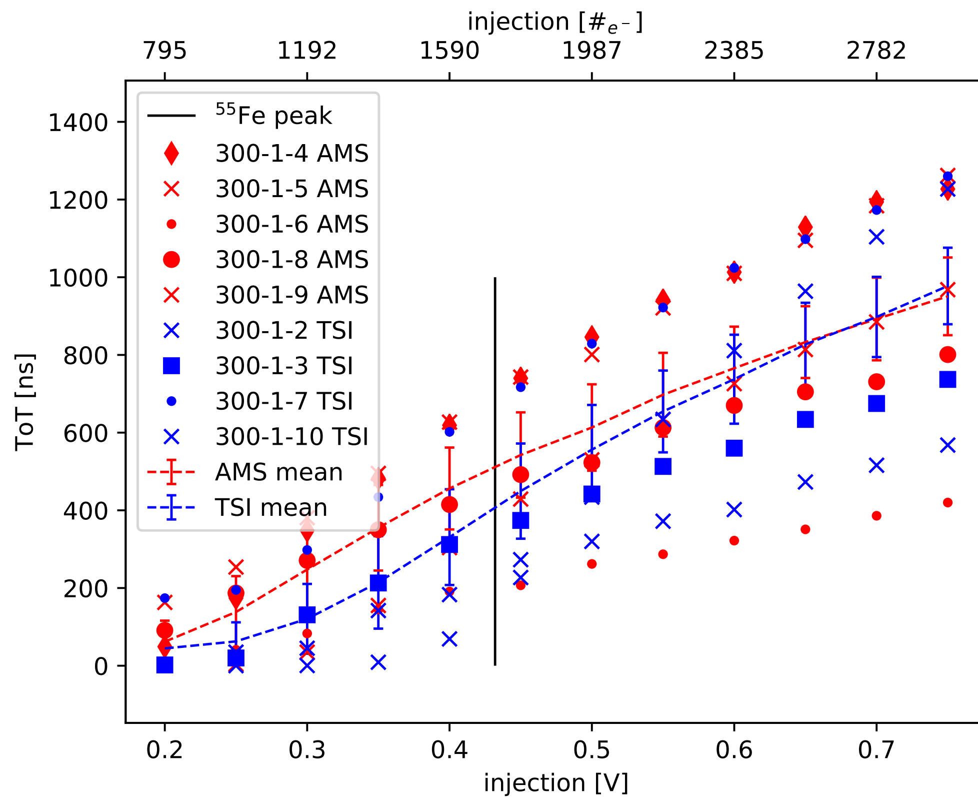

Figure A2.: Injection scan for all sensors around ^{55}Fe equivalent voltage of 0.42 V.

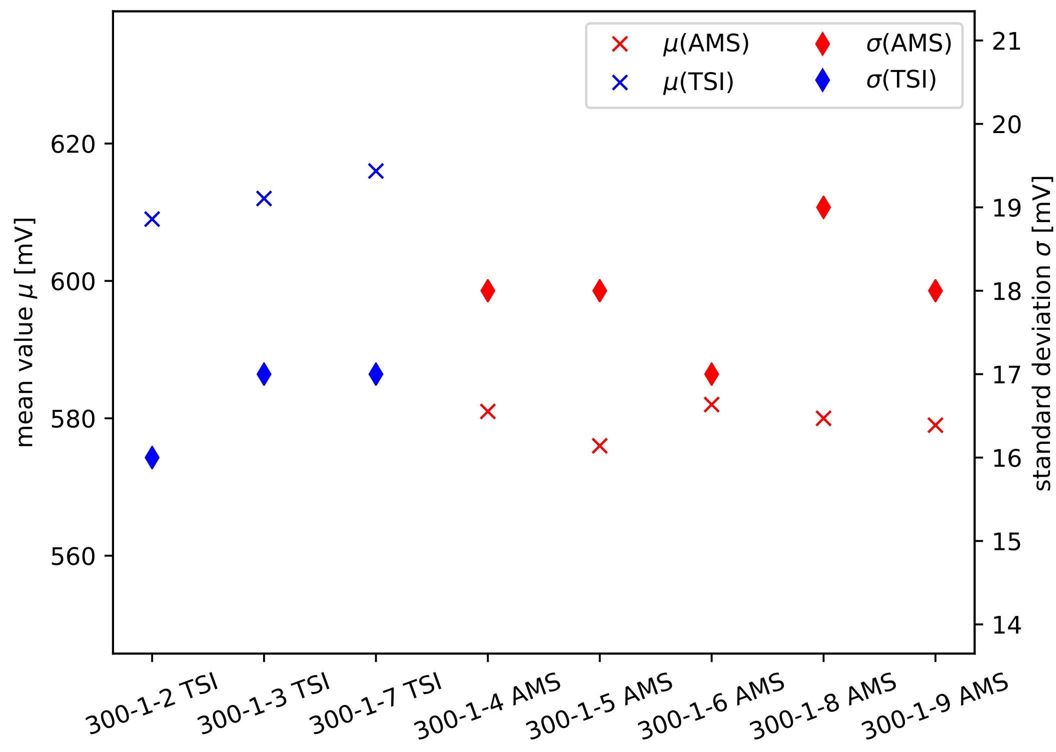

Figure A3.: Fitted input parameters for SNR calculation measured at a baseline of $b = 800\,\mathrm{mV}$.

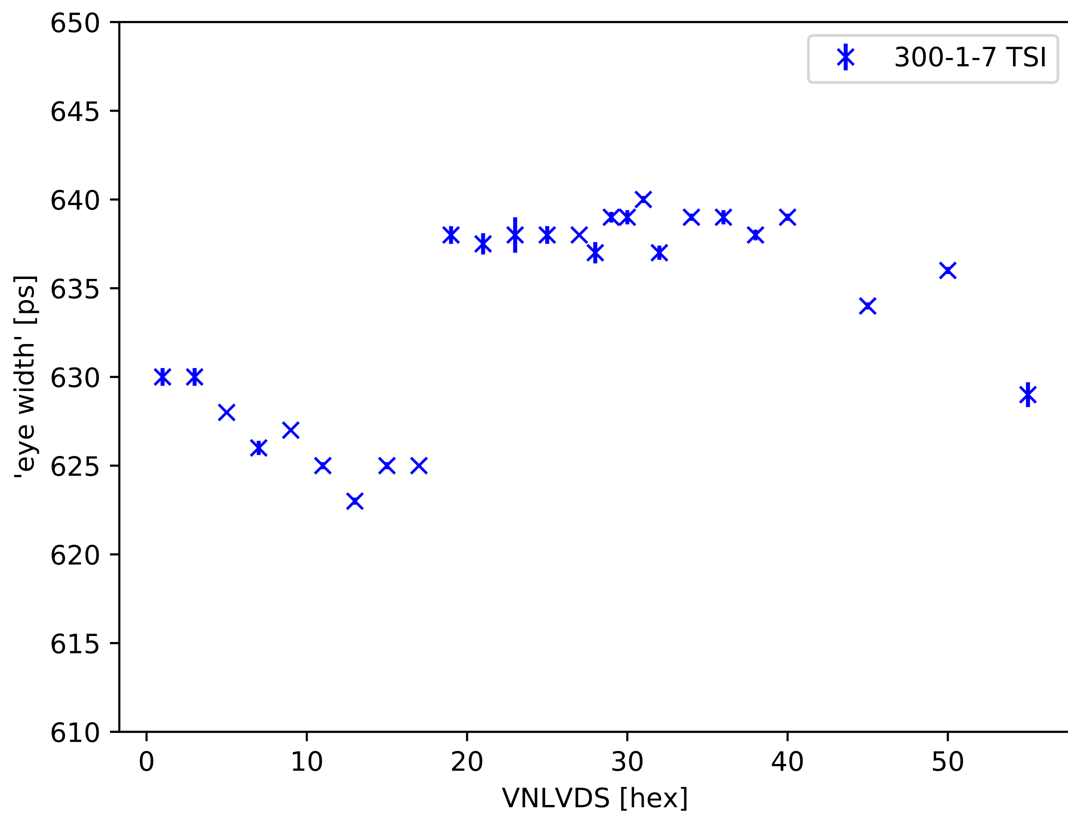

Figure A4.: ‘eye width’ measured versus VNLVDS.

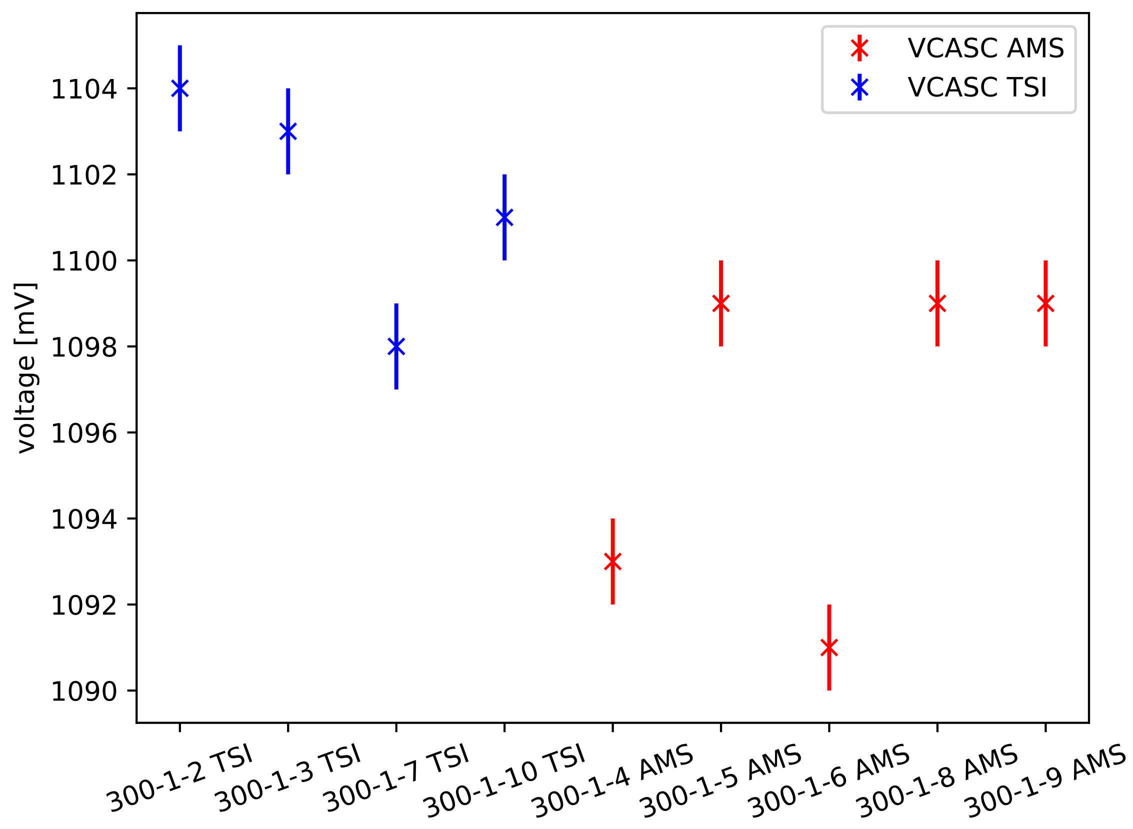

Figure A5.: VCASC measured for all tested sensors.

Bibliography

[1] A. Blondel *et al.* (Mu3e Collaboration). *Research Proposal for an Experiment to Search for the Decay $\mu \rightarrow eee$*. **2013**. 1301.6113.

[2] Mark Thomson. *Modern particle physics*. Cambridge University Press, Cambridge [u.a.], **2013**. ISBN: 978-1-107-03426-6 and 1-107-03426-4.

[3] G. Arnison *et al.* *Experimental observation of isolated large transverse energy electrons with associated missing energy at s=540 GeV*. Physics Letters B, **122**, 1: pp. 103 – 116, **1983**. ISSN: 0370-2693. doi:https://doi.org/10.1016/0370-2693(83)91177-2. URL: http://www.sciencedirect.com/science/article/pii/0370269383911772.

[4] Serguei Chatrchyan *et al.* (CMS). *Observation of a new boson at a mass of 125 GeV with the CMS experiment at the LHC*. Phys. Lett., **B716**: pp. 30–61, **2012**. doi:10.1016/j.physletb.2012.08.021. 1207.7235.

[5] G. Hernández-Tomé, G. López Castro and P. Roig. *Flavor violating leptonic decays of τ and μ leptons in the Standard Model with massive neutrinos*. Eur. Phys. J., **C79**, 1: p. 84, **2019**. doi:10.1140/epjc/s10052-019-6563-4. 1807.06050.

[6] Ivan Perić. *A novel monolithic pixelated particle detector implemented in high-voltage CMOS technology*. Nuclear Instruments and Methods in Physics Research, **582**, 3: pp. 876 – 885, **2007**. ISSN: 0168-9002. doi:https://doi.org/10.1016/j.nima.2007.07.115. VERTEX 2006, URL: http://www.sciencedirect.com/science/article/pii/S0168900207015914.

[7] ams AG. *High Voltage CMOS process*. Accessed: 2019-01-07, URL: https://ams.com/process-technology#highvoltagecmos.

[8] TSI Semiconductors. *TSI process overview*. Accessed: 2019-01-07, URL: http://www.tsisemi.com/process/.

[9] D. Immig. *Characterization of ATLASPix1, an HV-CMOS Demonstrator for the Phase-II Upgrade of the ATLAS Inner Tracker*. Master's thesis, Heidelberg University, **2019**.

[10] John McDowall. *High scale boundary conditions in extensions of the standard model*. Master's thesis. URL: http://theses.gla.ac.uk/41082/.

[11] Edward Kearns *et al.* *Detecting Massive Neutrinos*. Scientific America Inc., **Aug 1999**. doi:10.1016/j.cpc.2009.08.005.

URL: http://nngroup.physics.sunysb.edu/~chiaki/BMCC/Mentor/DetectingMassiveNeutrinoSciAm99.pdf.

[12] Q.-R. Ahmad. *Measurement of the Rate of $\nu_e + d$ & $p + p + e^-$ Interactions Produced by ^8B Solar Neutrinos at the Sudbury Neutrino Observatory.* **87**: 071301, **Aug 2001**. doi:10.1103/PhysRevLett.87.071301. nucl-ex/0106015.

[13] Takehiko Asaka and Mikhail Shaposhnikov. *The νSM, dark matter and baryon asymmetry of the universe. Phys. Lett.*, **B620**: pp. 17–26, **2005**. doi:10.1016/j.physletb.2005.06.020. URL: http://infoscience.epfl.ch/record/151084.

[14] Yoshitaka Kuno and Yasuhiro Okada. *Muon decay and physics beyond the standard model. Rev. Mod. Phys.*, **73**: pp. 151–202, **2001**. doi:10.1103/RevModPhys.73.151. hep-ph/9909265.

[15] William J. Marciano, Toshinori Mori and J. Michael Roney. *Charged Lepton Flavor Violation Experiments. Annual Review of Nuclear and Particle Science*, **58**, 1: pp. 315–341, **2008**. doi:10.1146/annurev.nucl.58.110707.171126. URL: https://doi.org/10.1146/annurev.nucl.58.110707.171126.

[16] U. Bellgardt *et al. Search for the decay $\mu^+ \to e^+e^+e^-$. Nuclear Physics B*, **299**, 1: pp. 1 – 6, **1988**. ISSN: 0550-3213. doi:https://doi.org/10.1016/0550-3213(88)90462-2. URL: http://www.sciencedirect.com/science/article/pii/0550321388904622.

[17] Toshinori Mori (MEG). *Final Results of the MEG Experiment. Nuovo Cim.*, **C39**, 4: p. 325, **2017**. doi:10.1393/ncc/i2016-16325-7. 1606.08168.

[18] W. Bertl *et al. A search for μ-e conversion in muonic gold. The European Physical Journal C - Particles and Fields*, **47**, 2: pp. 337–346, **Aug 2006**. ISSN: 1434-6052. doi:10.1140/epjc/s2006-02582-x. URL: https://doi.org/10.1140/epjc/s2006-02582-x.

[19] R. H. Bernstein (Mu2e Collaboration). *The Mu2e Experiment. Front.in Phys.*, **7**: p. 1, **2019**. doi:10.3389/fphy.2019.00001. 1901.11099.

[20] Frank Thuselt. *Physik der Halbleiterbauelemente.* Springer Spektrum, Berlin, Heidelberg, **2018**, 3. aufl. 2018 edition. ISBN: 978-3-662-57638-0. doi:10.1007/978-3-662-57638-0. URL: https://doi.org/10.1007/978-3-662-57638-0.

[21] Hermann Kolanoski and Norbert Wermes. *Teilchendetektoren.* Springer Spektrum, Berlin, Heidelberg, **2016**, 1. aufl. 2016 edition. ISBN: 978-3-662-45350-6. doi:10.1007/978-3-662-45350-6. URL: http://dx.doi.org/10.1007/978-3-662-45350-6.

[22] A. Weber. *Entwurf eines Pixelsensorchips für die Teilchenphysik.* Master's thesis, Karlsruher Institut für Technologie, **2016**.

[23] A. Hierlemann, Henry Baltes *et al. Integrated Chemical Microsensor*

Systems in CMOS Technology. (pp. Online–Ressource (IX, 229 p. 125 illus, digital)), **2005**. doi:10.1007/b138987. URL: http://dx.doi.org/10.1007/b138987.

[24] A. M. Gonzalez. *TCAD Simulation of the MuPix7 sensor for the Mu3e Pixel Tracker.* DPG Spring Meeting, **2019**. URL: https://www.psi.ch/sites/default/files/import/mu3e/TalksEN/DPG18_Meneses.pdf/.

[25] Shihong Ouyang *et al. Surface Patterning of PEDOT:PSS by Photolithography for Organic Electronic Devices.* Journal of Nanomaterials, **2015**, **07 2015**. doi:10.1155/2015/603148.

[26] K.A. Olive and Particle Data Group. *Improved procedure for calculating the collision stopping power of elements and compounds for electrons and positrons.* Chinese Phys. C, **38**, 9, **2014**. URL: https://iopscience.iop.org/article/10.1088/1674-1137/38/9/090001.

[27] Stephen M. Seltzer and Martin J. Berger. *Improved procedure for calculating the collision stopping power of elements and compounds for electrons and positrons.* The International Journal of Applied Radiation and Isotopes, **35**, 7: pp. 665 – 676, **1984**. ISSN: 0020-708X. doi:https://doi.org/10.1016/0020-708X(84)90113-3. URL: http://www.sciencedirect.com/science/article/pii/0020708X84901133.

[28] D. Immig. *Charakterisierung des VCO, der PLL und der Pulsform des MuPix7 in Abhängigkeit der Umgebungstemperatur.* Bachelor's thesis, Heidelberg University, **2016**.

[29] L. Rossi *et al. Pixel Detectors.* Particle Acceleration and Detection. Springer, Berlin ; Heidelberg [u.a.], **2006**. ISBN: 3-540-28332-3 and 978-3-540-28332-4.

[30] Ivan Peric. *A novel monolithic pixelated particle detector implemented in high-voltage CMOS technology.* Nucl. Instrum. Meth., **A582**: pp. 876–885, **2007**. doi:10.1016/j.nima.2007.07.115.

[31] Heiko Augustin *et al. The MuPix System-on-Chip for the Mu3e Experiment.* Nucl. Instrum. Meth., **A845**: pp. 194–198, **2017**. 1603.08751.

[32] H. Augustin. *Pixel Design.* Private Communication, **2019**.

[33] H. Augustin. *Characterization of a novel HV-MAPS Sensor with two Amplification Stages and first examination of thinned MuPix Sensors.* Master's thesis, Heidelberg University, **2014**.

[34] S. Dittmeier. *Fast data acquisition for silicon tracking detectors at high rates.* Ph.D. thesis, Heidelberg University, **2018**.

[35] L. Huth. *Development of a Tracking Telescope for Low Momentum Particles and High Rates consisting of HV-MAPS.* Master's thesis, Heidelberg University, **2014**.

[36] A. Schmidt. *Schematic of the MuPix7 insert.* Technical report. Accessed:

2019-02-07, URL: https://www.physi.uni-heidelberg.de/Forschung/he/mu3e/wiki/images/4/49/MuPix7_Insert_Schematic.pdf.

[37] Hamamatsu Photonics K.K.®. *MPPC ® (Multi-Pixel Photon Counter)*. Accessed: 2019-03-07, URL: https://www.hamamatsu.com/resources/pdf/ssd/s13360_series_kapd1052e.pdf.

[38] J. Hammerich. *Studies of HV-MAPS analog performance*. Bachelor's thesis, Heidelberg University, **2015**.

[39] L. Huth. *A High Rate Testbeam Data Acquisition System and Characterization of High Voltage Monolithic Active Pixel Sensors*. Ph.D. thesis, Heidelberg University, **2018**.

[40] Intel. *Stratix IV GT FPGA Features*. Accessed: 2019-02-07, URL: https://www.intel.com/content/dam/www/programmable/us/en/pdfs/literature/pt/stratix-iv-product-table.pdf.

[41] DOGA Limited. *BINDER MK Series Environmental Simulation Chambers*. Accessed: 2019-03-07, URL: http://www.dogalimited.com/en/product/binder-mk-series-environmental-simulation-chambers-mk53-mk115-mk240-mk720-.

[42] A. Perrevoort. *Sensitivity Studies on New Physics in the Mu3e Experiment and Development of Firmware for the Front-End of the Mu3e Detector*. Ph.D. thesis, Heidelberg University, **2018**.

[43] A. M. Gonzalez. *TCAD simulations*. Group Talk, **2019**.

[44] C. D. Motchenbacher and Franklin C Fitchen. *Low-noise electronic design, by C. D. Motchenbacher and F. C. Fitchen*. Wiley New York, **1973**. ISBN: 0471619507.

[45] Tektronix. *Digital Phosphor Oscilloscopes - DPO7000C Series Datasheet*.

[46] Helmuth Spieler. *Semiconductor detector systems*. ARRAY(0x5076a68). Oxford Univ. Press, Oxford [u.a.], **2008**. ISBN: 978-0-19-852784-8.

[47] A. Blondel *et al.* (Mu3e Collaboration). *Mu3e technical design report. Mu3e internal note*, **2017**.

Erklärung

Ich versichere hiermit, dass ich diese Arbeit selbstständig verfasst und keine anderen als die angegebenen Quellen und Hilfsmittel benutzt habe.

Heidelberg, den 26. Mai 2019,

Christoph Aram Blattgerste

Danksagung

Die letzte Seite all denen widmen, die mich bei der Durchführung und dem Aufschrieb meiner Bachelorarbeit gefördert und so zum Gelingen beigetragen haben.

An erster Stelle möchte ich Prof. Dr. André Schöning für die Erläuterungen zum Mu3e Experiments, mit der ich meine Bachelorarbeit begann und ebenso für die Begutachtung meiner Abschlussarbeit danken, mit der ich meinen wissenschaftichen Weg beginnen durfte.

Auch gilt mein Dank meiner Zweitkorrektorin Prof. Dr. Silvia Masciochhi, die ich vom Mu3e Experiment überzeugen durfte.

Mein Betreuer Heiko Augustin und besonders auch David Immig standen mir besonders bei der Planung, Durchführung und Auswertung der Experimente stes mit Rat und Tat zur Seite.

Herzlich danken will ich auch allen meinen Kollegen der Mu3e Arbeitsgruppe: Lars, Sebastian, Thomi, Jan, Adrian, Benni, Annie, Luigi, Frank und Lennart. Die Arbeit im Labor und auf diversen Testbeam Kampagnen hat mir von Tag zu Tag wieder Freude bereitet. Die vielen (mest) hilfreichen Kommentare von allen haben maßgeblich zum Gelingen meines Projekts beigetragen.

Am Schluss möchte ich von ganzem Herzen meiner Familie und meinen Freunden danken, die mich bei meiner Bachelorarbeit, wie auch in meinem gesamten Bachelorstudium durch dumme Fragen und sehr hilfreiche Tipps zum Nachdenken angeregt haben. Es macht immer wieder Spaß, euch die Physik zu erklären.